



**HAL**  
open science

## Laboratory experiments to unveil the molecular reactivity occurring during the processing of ices in the protosolar nebula

Thomas Gautier, G. Danger, O. Mousis, F. Duvernay, V. Vuitton, L. Flandinet, R. Thissen, F.-R. Orthous-Daunay, A. Ruf, T. Chiavassa, et al.

### ► To cite this version:

Thomas Gautier, G. Danger, O. Mousis, F. Duvernay, V. Vuitton, et al.. Laboratory experiments to unveil the molecular reactivity occurring during the processing of ices in the protosolar nebula. *Earth and Planetary Science Letters*, 2020, 531 (1 February), pp.art. 116011. 10.1016/j.epsl.2019.116011 . hal-02396048

**HAL Id: hal-02396048**

**<https://hal.science/hal-02396048>**

Submitted on 5 Dec 2019

**HAL** is a multi-disciplinary open access archive for the deposit and dissemination of scientific research documents, whether they are published or not. The documents may come from teaching and research institutions in France or abroad, or from public or private research centers.

L'archive ouverte pluridisciplinaire **HAL**, est destinée au dépôt et à la diffusion de documents scientifiques de niveau recherche, publiés ou non, émanant des établissements d'enseignement et de recherche français ou étrangers, des laboratoires publics ou privés.

1 **Laboratory experiments to unveil the molecular reactivity occurring**  
2 **during the processing of ices in the protosolar nebula**

3 T. Gautier<sup>1,2\*</sup>, G. Danger<sup>\*,2</sup>, O. Mousis<sup>3</sup>, F. Duvernay<sup>2</sup>, V. Vuitton<sup>4</sup>, L. Flandinet<sup>4</sup>, R. Thissen<sup>5</sup>,  
4 F.-R. Orthous-Daunay<sup>4</sup>, A. Ruf<sup>2</sup>, T. Chiavassa<sup>2</sup>, L. S. d'Hendecourt<sup>2</sup>

5

6 <sup>1</sup> LATMOS, CNRS, Sorbonne Université, Université Versailles St-Quentin, UMR8190, 11 bvd  
7 d'Alembert F-78280 Guyancourt, France

8 <sup>2</sup> Aix-Marseille Université, PIIM UMR-CNRS 7345, F-13397 Marseille, France

9 <sup>3</sup> Aix-Marseille Université, CNRS, LAM (Laboratoire d'Astrophysique de Marseille) UMR 7326,  
10 F-13388, Marseille, France

11 <sup>4</sup> Université Grenoble Alpes, CNRS, IPAG, Grenoble F-38000, France

12 <sup>5</sup> Laboratoire de Chimie Physique, CNRS, Université Paris-Sud et Paris-Saclay, UMR 8000, F-  
13 91405 Orsay, France.

14 \*Corresponding authors : [thomas.gautier@latmos.ipsl.fr](mailto:thomas.gautier@latmos.ipsl.fr) ; [gregoire.danger@univ-amu.fr](mailto:gregoire.danger@univ-amu.fr)

15

16 Running title: Organic Matter Evolution in the protosolar nebula

17 Keywords: Protosolar Nebula, Interstellar Ices, Organic Matter, Laboratory simulations, High  
18 Resolution Mass Spectrometry.

19 **Abstract**

20 Using laboratory experiments, we investigate the role of photo and thermal degradation in  
21 the possible complexification mechanisms of organic matter that may originate from  
22 interstellar ices prior to, or during the formation of the Solar System. We perform High  
23 Resolution Orbitrap Mass Spectrometry on organic residues formed from the photo- and  
24 thermochemical alterations of Interstellar Medium (ISM) dirty ice laboratory analogues. We  
25 probe, at the molecular level, the possible effects within the protosolar nebula on the  
26 composition and structure of these organic refractory materials obtained from an initial ice  
27 composition representative of astrophysical ices. We show that nitrogen incorporation, by  
28 competing with the carbon, has a strong influence on the final composition of the residue.  
29 NH<sub>3</sub> rich ices lead to a group of unsaturated molecules in the final residue, while H<sub>2</sub>O rich ices  
30 lead to saturated ones. Finally, we observe and discuss the strong effect of UV irradiation on  
31 the decarboxylation on organic matter and discuss potential implications of this result for the  
32 protosolar nebula.

33

34

35

36

37

38

39

40 **1. Introduction**

41 The organic content of the solar system small bodies such as comets, asteroids or meteorites  
42 found on Earth, has been an ongoing field of study for decades. One of the interest of such  
43 study is that the organic matter content of these bodies can be used as a tracer to unveil their  
44 history. Such organic matter can be, at least partially, inherited from the organic matter  
45 formed in the interstellar medium (ISM) prior to the protosolar nebula (PSN) formation. In this  
46 regard, understanding the chemistry occurring during the photo and thermal processing of  
47 astrophysical ices is a key aspect to apprehend the primitive organic contents of the small  
48 bodies and the history of the solar system.

49 Ices are observed in a wide range of objects, from dense molecular clouds (Boogert et al.,  
50 2008) to comets/asteroids or icy satellites of giant planets such as Europa or Enceladus (Clark  
51 et al., 2013). The ice organic content can be obtained by their in situ analysis (*e.g.* Goesmann  
52 et al., 2015), infrared remote sensing (*e.g.* De Sanctis et al., 2017) or inferred from molecules  
53 detected in the gas phase of objects (*e.g.* Meech and Svoren, 2004). However, such  
54 information remains sparse, difficult to obtain and with limited knowledge of the alteration  
55 processes (aqueous, thermal or by irradiation) undergone by the organic matter analyzed. In  
56 contrast, the soluble organic matter (SOM) in meteorites has been extensively studied and  
57 displays a wide variety of organic matter, such as hydroxy and amino acids, sugar derivatives  
58 and hydrocarbons (Burton et al., 2014; Callahan et al., 2014; Cooper et al., 2001; Cronin and  
59 Moore, 1971; Martins et al., 2015; Pizzarello and Shock, 2010a).

60 For a few decades, laboratory simulations have been developed to bridge the gap between  
61 the organic matter observed in astrophysical ices and the one observed in meteorites. In this  
62 work, we use such an experimental approach to investigate the chemistry of organic

63 molecules that could be (trans-) formed from interstellar ices in the PSN and later  
64 incorporated in the meteorites parent bodies.

65 Laboratory ice processing has been shown to form refractory organic residues – also called  
66 *yellow stuff* - if reduced carbon such as methanol or methane is present, in addition to H<sub>2</sub>O  
67 and NH<sub>3</sub>, in the initial ice (Bernstein et al., 1995; Briggs et al., 1992). A wide molecular diversity  
68 was inferred in these residues by infrared analyses (Muñoz Caro and Schutte, 2003). Bernstein  
69 et al., (1995) showed that infrared bands relative to nitrogen functional groups increase when  
70 the quantity of NH<sub>3</sub> increases in the ice, while increasing H<sub>2</sub>O in the initial ice results in residues  
71 presenting similar signatures to the ones of residues formed from NH<sub>3</sub> rich ices (Henderson  
72 and Gudipati, 2015; Nuevo et al., 2011). The formation of such organic residue is also of high  
73 interest for astrobiology, in particular de Marcellus et al., (2015) and Meinert et al., (2016)  
74 reported the formation aldehyde and sugars such as ribose and other related sugars in the  
75 residue.

76 A direct snapshot of the residue molecular diversity was obtained by high resolution mass  
77 spectrometry (HRMS) (Danger et al., 2013) where thousands of molecules presenting masses  
78 up to several thousands of Da were detected. Previous work from our group showed that  
79 residues are formed with two distinctive distributions for the organic matter, one enriched in  
80 nitrogen, with an average nitrogen to carbon ratio of 1.3, and another one presenting  
81 molecules predominantly with a carbon skeleton (Fresneau et al. 2017).

82 In this contribution, we analyze the molecular content using HRMS and infrared spectroscopy  
83 of organic residues formed through the irradiation and warming of several types of  
84 H<sub>2</sub>O:CH<sub>3</sub>OH:NH<sub>3</sub> ices. We mainly focus on the chemistry of ammonia and on the rapid decay

85 of carboxyls functions under UV irradiation in the protosolar ice, in apparent contradiction  
86 with the large amount of carboxyls found in meteorites.

## 87 **2. Materials and Methods**

### 88 2.1. Sample Synthesis

89 In this work we investigate the processing of ice layers, analogs to organic rich protosolar  
90 grains, into organic residues under photo and thermal alterations. The experimental setup  
91 used to produce these laboratory analogs has been described in detail in Nuevo et al., 2007.  
92 The samples analyzed for the present work were the ones used by Fresneau et al. 2017 to  
93 investigate the relationship between cometary materials and interstellar ices at a  
94 macromolecular level. The main characteristics of the setup and of the samples are recalled  
95 here. To produce the analogs, water, ammonia and methanol were mixed in a stainless-steel  
96 line before injection into the deposition chamber. The H<sub>2</sub>O was purified with a Millipore Direct  
97 Q5 system. The high purity CH<sub>3</sub>OH (99.9%) and NH<sub>3</sub> (99.98%) were purchased from Aldrich and  
98 Messer, respectively. To investigate the effect of the original ice composition on the molecular  
99 complexification of the organics in the sample, different ratios of water ammonia and  
100 methanol were used for this study and are given in Table 1. To form the analog samples, ices  
101 were deposited under vacuum ( $10^{-5}$  Pa) on a MgF<sub>2</sub> substrate cryogenically cooled down to 77K.  
102 The ices were irradiated with VUV photons (principally Ly- $\alpha$ , at 121.5 nm) simultaneously to  
103 its deposition on the substrate using a hydrogen discharge lamp emitting  $2 \times 10^{14}$  photons.cm<sup>-2</sup>.s<sup>-1</sup>.  
104 This rate corresponds to an average of 2 Ly $\alpha$  photons interacting with each deposited  
105 molecule during the sample production. The photon-molecule interaction occurs  
106 predominantly in the bulk ice and not before the molecules condensation. The ice deposition  
107 and irradiation processes were performed for 48h, after which the deposition and irradiation

108 were stopped and the MgF<sub>2</sub> substrate slowly warmed up to room temperature at  $1.7 \times 10^{-3}$   
109 K.s<sup>-1</sup> using a thermal regulator (335 Temperature Controller from LakeShore) on the cryogenic  
110 head. The sample was monitored during its formation using a FT-IR spectrometer attached to  
111 the deposition chamber. The mid-infrared spectra (4000-1000 cm<sup>-1</sup>, sum of 500 scans and a  
112 resolution of 2 cm<sup>-1</sup>) were used to ensure the proper deposition rate and composition of the  
113 ice, as well as to give information about the organic residue composition left on the substrate  
114 after the ice warm-up (de Marcellus et al., 2017). These residues obtained in the laboratory  
115 are considered analogs of the organic residues formed by the processing of icy mantles on  
116 interstellar grains during the solar system formation. To investigate the effect of UV dose  
117 received by the organic residue during its lifetime inside proto-planetary disks, three samples  
118 were additionally over-irradiated at room temperature during 48 hours without further  
119 deposition and after their warm-up to room temperature and 10<sup>-5</sup> Pa, considerably increasing  
120 the irradiation dose imparted per bond to around 10keV (de Marcellus et al, 2017). After their  
121 synthesis, all samples were retrieved under inert atmosphere (Argon) sample holders to  
122 prevent contamination. Given the extremely low amount of material formed during these  
123 experiments, a quantitative production yield was not determined. However, we can  
124 qualitatively assess the production rates relatively to each other by comparing their  
125 absorbance spectra, as described in Fresneau et al. 2017. Using this approach, the sample  
126 with the highest production yield was the H<sub>2</sub>O:CH<sub>3</sub>OH:NH<sub>3</sub> 3:1:1 sample, followed by the NH<sub>3</sub>-  
127 poor ices 10:1:1 and 3:1:0.2 which have similar residue production yield. However, the NH<sub>3</sub>-  
128 rich ice 3:1:5 is by far the one yielding the less organic residue as discussed in Fresneau et al.  
129 2017.

130 **Table 1: List of samples and their production parameter used for this study. Molecules are**  
131 **considered detected in the samples only if they are present in all replicates.**

<b>H<sub>2</sub>O:CH<sub>3</sub>OH:NH<sub>3</sub> ratio</b>	<b>Over-Irradiation of the sample</b>	<b>Number of replicates</b>
<b>3:1:1</b>	-	3
<b>3:1:1</b>	48 hrs	3
<b>3:1:5</b>	-	2
<b>3:1:0.2</b>	-	3
<b>10:1:1</b>	-	3

132

133 **2.2. Sample Analysis and data treatment**

134 **2.2.1. *Orbitrap High resolution mass spectrometry***

135 To access their molecular composition, samples were analyzed through high-resolution mass  
136 spectrometry (HRMS) using an LTQ Orbitrap XL. Residues were dissolved in 250  $\mu$ L of ultrapure  
137 methanol. All residues were totally soluble in methanol except the over-irradiated ones that  
138 contained a non-soluble fraction (Fresneau et al. 2017, de Marcellus et al. 2017). Note that  
139 only the soluble fraction of these residues in methanol can be analyzed by HRMS with ESI  
140 ionization. The exact solubilization protocol can be found in Fresneau et al. 2017. The  
141 instrument was equipped with an electrospray ionization source (ESI). Instrument parameters  
142 used were: syringe flow rate: 3  $\mu$ L.min<sup>-1</sup>; needle voltage: 3.7 kV; capillary temperature: 275°C;  
143 tube lens voltage: respectively -131 V and +90 V for the negative and positive ionization  
144 modes; resolution was set at 100,000 at  $m/z$  400; actual resolution was of 120 000 at  $m/z$  200  
145 and reached 220 000 at  $m/z$  400; the mass acquisition range:  $m/z$  200-400. The instrument  
146 was externally calibrated using a mix of caffeine, MRFA peptides and Ultramark.

147 **2.2.2. *Data processing***

148 The data were acquired with the XCalibur software and then post-calibrated and processed  
149 through Attribution, and in-house software developed at IPAG specifically for the processing  
150 and interpretation of high-resolution mass spectrometry data.

151 In order to avoid mis-attribution of peaks and discussing non relevant signal, we chose to be  
152 extremely conservative in the attribution of the peaks. We thus keep peaks for which we had  
153 a completely unambiguous attribution. This lead to discard peaks for which an isobaric  
154 ambiguity may have existed and peaks for which the signal-to-noise ratio (i.e. number of ions  
155 in the cell) was low enough to affect the mass accuracy of the Orbitrap. This lead us to a sharp  
156 decrease between the number of detected peaks and the number of attributed ones. For  
157 example, for the 3:1:1 sample, there was ~35000 detected peaks, most of them having a very  
158 low signal to noise ratio ( $S/N < 3$ ); amongst the detected peaks, 1168 were at sufficient S/N  
159 ratio and resolution to limit low ion counts and isobaric effects and were successfully and  
160 unambiguously attributed to a molecular formula. We did not detect any significant variation  
161 in the ratio of attributed peaks versus detected peaks with the samples studied. All samples  
162 were treated following exactly the same data treatment to ensure no bias would be  
163 introduced.

### 164 *2.2.3. Modified van Krevelen Diagrams*

165 van Krevelen diagrams were originally introduced in the 50's for petroleomics and present a  
166 scatter plot of the oxygen to carbon ratio versus hydrogen to carbon ratio of the sample  
167 elementary composition (van Krevelen, 1950). This visualization is especially adapted to  
168 investigate structural changes in complex samples such as petroleum (Kim et al., 2003; Wu et  
169 al., 2004) and has been adapted in so-called 'modified van Krevelen' for the study of planetary  
170 interest constituted of several thousands of molecules of unknown composition (Danger et

171 al., 2016; Gautier et al., 2014; Pernot et al., 2010; Ruf et al., 2017; Somogyi et al., 2012). It  
172 should be underlined here that although van Krevelen or modified van Krevelen diagrams  
173 present visible linear alignments of structures, these alignments cannot be directly linked to  
174 the structure of the material but simply reflect the intrinsic order of the C, H, N and O  
175 compositional space (Hertkorn et al., 2008).

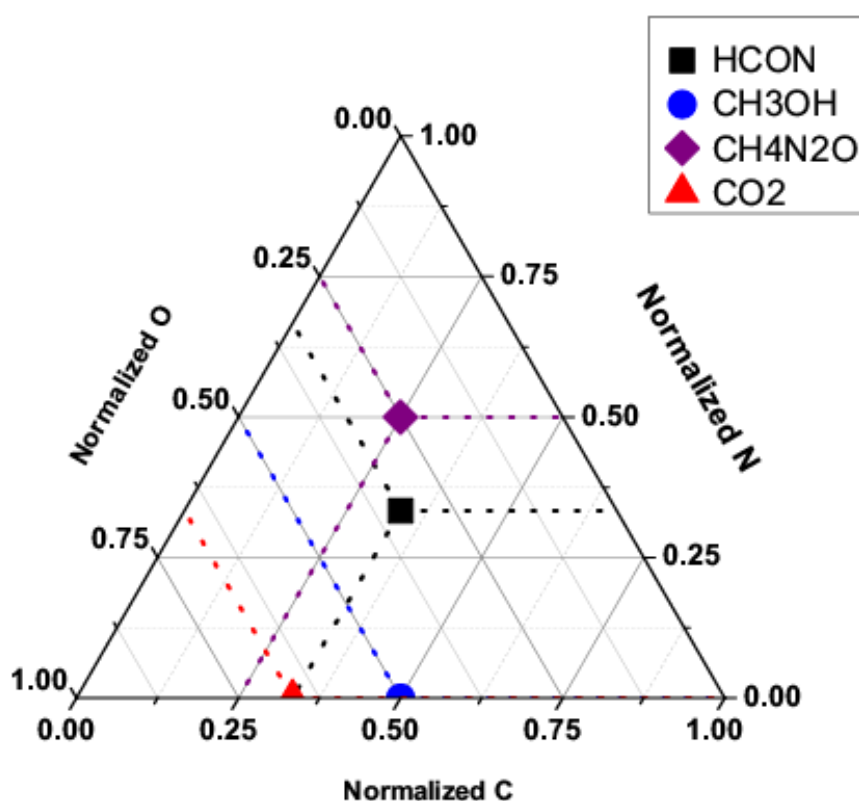
#### 176 *2.2.4. Ternary space diagrams*

177 van Krevelen diagrams allow for the discrimination of samples along two dimensions of the  
178 parameter space. This can limit the separation of samples presenting little divergence, in  
179 which case a representation using three dimensions could be necessary. A step forward was  
180 made using the  $m/z$  of the molecules as third dimension in 3D van Krevelen Diagrams (Wu et  
181 al., 2004, Pernot et al. 2010, Gautier et al. 2014, Danger et al. 2016) but these 3D diagrams  
182 demonstrated to be impractical to use as they require a user-defined orientation, which  
183 introduces a bias in the representation.

184 We introduce here a visualization for complex organic matter using a mix of modified van  
185 Krevelen diagrams and ternary space representations. These ternary space representations  
186 were introduced in the 18<sup>th</sup> century for the study of color mixing (Newton, 1704) and are now  
187 commonly used in Geology, Chemistry and Material Sciences (Howarth, 1996). This  
188 visualization can be defined as follows: each of the molecules present in the sample is located  
189 in a three-parameter triangular space with non-orthogonal axes. In this work we chose each  
190 axis to respectively bear information about the oxygen, carbon and nitrogen content, of the  
191 molecules. This means that the representation presented here focuses on the large scale  
192 structure of the macromolecules and does not bear information about the hydrogen content  
193 or the double bond equivalent of the molecules. Should such information be needed, a way

194 to mitigate this issue would be to use Hydrogen content as axis instead of carbon, nitrogen or  
195 oxygen.

196 The position of a given molecule in the diagram can be defined so that its projection on each  
197 axis relatively to an atom  $\alpha$  (with  $\alpha = \text{C, N or O}$ ) is be equal to  $\frac{\alpha}{\text{C+N+O}}$ . An example of this  
198 representation is given in Figure 1.



199  
200 **Figure 1 : Example of ternary space molecular diagram and the position of four molecules in this**  
201 **diagram. The black square shows the position of a molecule of composition HCON, the blue circle a**  
202 **molecule of CH<sub>3</sub>OH, the red triangle would be CO<sub>2</sub> and the purple diamond a molecule of formula**  
203 **CH<sub>4</sub>N<sub>2</sub>O. The colored dashed lines are the projection of each point on the three axes to facilitate the**  
204 **interpretation of the diagram.**

205 The black square shows the position of a molecule of composition HCON which has an equal  
206 number of carbon, nitrogen and oxygen atoms, each axis thus has a 1/3 weight in the position  
207 of the molecule. The blue circle shows the position of methanol (CH<sub>3</sub>OH, or also CO,  
208 formaldehyde H<sub>2</sub>CO or acetic acid CH<sub>3</sub>COOH) where O and C are equals. The red triangle shows

209 the position of CO<sub>2</sub> and the purple diamond would be the location of a molecule with raw  
210 formulae CH<sub>4</sub>N<sub>2</sub>O. Since this visualization requires the normalization of the molecular ratios  
211 to the sum of C+N+O atoms, the position of a point on an axis should not be read as the  
212 molecular composition of this molecule.

### 213 2.2.5. Structural markers

214 The formulas of organic molecules, available thanks to the use of high-resolution mass  
215 spectrometry, can be used to infer structural information about the molecules detected in the  
216 samples. A structural marker extensively used in the literature is the Double Bond Equivalent  
217 (DBE), which gives information regarding the unsaturation (double bonds and cycles) borne  
218 by a molecule in its structure. The DBE is calculated as follows:  $DBE = \frac{1}{2} (2C - H + N) + 1$   
219 where C, H and N represent respectively the number of carbon, hydrogen and nitrogen atoms  
220 within the molecule. The interpretation of DBE in itself is however difficult in the case of large  
221 molecules and/or molecules with a large number of heteroatoms such as the one present in  
222 our samples (Danger et al. 2016). In addition to the DBE we therefore also used the New  
223 Aromaticity Equivalent parameter  $X_c$  as defined by Yassine et al., 2014 :  $X_c = \frac{2C+N-H-2mO}{DBE-mO}$   
224 where  $m$  is the fraction of oxygen atoms in the conjugated structure of the molecules. Using  
225 infrared analysis of the residue Danger et al. 2016 estimated that the double bonded O atoms  
226 represented approximately 50% of the O atoms in the residue, giving an estimate of  $m=0.5$ .  
227 Should this value of  $m$  be slightly higher or lower, this would not affect the classification of the  
228 bulk of the molecules but simply shift the  $X_c$  distribution toward higher or lower values. The  $X_c$   
229 distribution for all samples is given in Figure SI 1.

230 For each molecule detected in the sample we calculated the DBE and  $X_c$ . Following Yassine et  
231 al. 2014 classification, molecules for which  $X_c > DBE$  are by essence aliphatic. If  $X_c < 2.5$ , the

232 molecules were considered as aliphatic; those with  $2.5 \leq X_c < 2.7$  were classified as aromatic  
233 and those for which  $X_c$  is greater than 2.7 as condensed aromatic.

### 234 **3. Results and discussion**

#### 235 3.1. Effect of Ammonia and water proportion in ices

##### 236 3.1.1. Influence of ammonia

237 Modified van Krevelen diagram H/C vs. N/C does not give sufficient information on the impact  
238 of the initial ammonia ice ratio as they rapidly become congested for such complex mixture of  
239 similar properties (Figure SI 8). We therefore used another representation that spreads the  
240 sample representation over three dimensions, the ternary space diagrams (Figure 2,  
241 respectively with H<sub>2</sub>O:CH<sub>3</sub>OH:NH<sub>3</sub> ratios of 3:1:5 blue circles and 3:1:0.2 red circles). Each dot  
242 in this diagram corresponds to the molecules detected in sample either in positive or in  
243 negative ionization mode. As inferred from this figure, both samples present a bi-modal  
244 distribution of their molecules. This bimodality is not related to the positive/negative  
245 ionization, but to the presence of a group of nitrogen-rich molecules in both samples. This N-  
246 rich fraction of the residue has already been observed by Fresneau et al. 2017 on the average  
247 composition of the residues. However, using elemental composition only, Fresneau et al. 2017  
248 were not able to provide an explanation for this N-rich distribution. We confirm here that this  
249 bimodality is clearly detected at the molecular level (bi-modal distributions for both samples  
250 in Figure 2), and we can use the ternary space diagram to investigate its origin. We can see in  
251 Figure 2 that for both residues the N-rich distributions are at higher N-axis and lower C-axis  
252 values relatively to the C-rich distribution. This corresponds to molecules with a higher

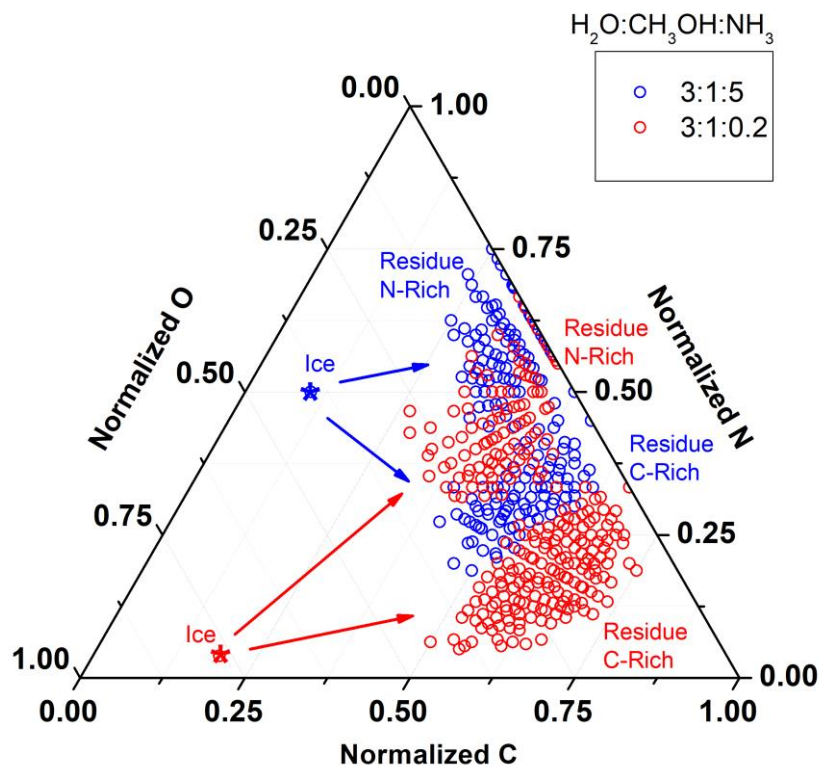


**Figure 2 : Ternary space diagrams of the molecules detected in positive and negative ionization mode in the sample produced with  $\text{H}_2\text{O}:\text{CH}_3\text{OH}:\text{NH}_3$  ratios of 3:1:5 (blue circles) and 3:1:0.2 (red circles). The areas at high N ratios correspond to the N-rich distribution identified by Fresneau et al. 2017 in the 3:1:5 and 3:1:0.2 samples respectively. The blue and red stars represent the position in the ternary space of the ice used to form the residue, respectively the  $\text{H}_2\text{O}:\text{CH}_3\text{OH}:\text{NH}_3$  3:1:5 and 3:1:0.2 ones. Colored arrows show the evolution pathway underwent by the organic matter from the ice to the formation of the residue.**

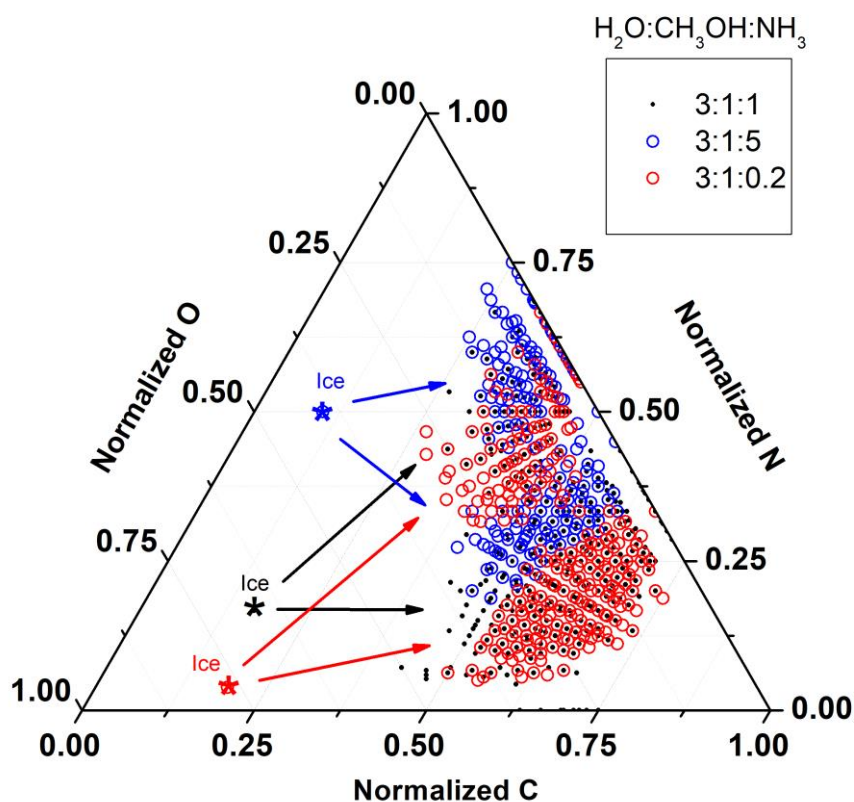
253 nitrogen content and lower carbon content (hence their names). But we can also see that  
 254 these distributions have a similar position on the O-axis, implying that the competition for  
 255 inclusion in the residue does not happen between N and O but between N and C. This indicates  
 256 that the difference between the carbon rich and the nitrogen rich group would be due to the  
 257 existence of nitrogen bearing functional groups with no oxygen or fewer carbon atoms, such  
 258 as cyclic or aromatic structures including nitrogen. See part 1.3 for further discussion on the  
 259 ice reactivity

260 For both initial ice mixtures, it appears that the residue formed contained far less oxygen  
 261 relatively to carbon and nitrogen than the original ice. This could be due to a large use of

262 carbon and nitrogen for the growth of the macromolecular structure, while oxygen would tend  
263 to inhibit polymeric or cyclic molecules formation. An unsurprisingly low reactivity of H<sub>2</sub>O in  
264 the residue formation could also explained these observations, implying that most of the O  
265 atoms in the residue comes from the methanol.

266 Interestingly, while there is almost no species in common in the distribution of the molecules  
267 detected in the residue formed from H<sub>2</sub>O:CH<sub>3</sub>OH:NH<sub>3</sub> ratios of 3:1:5 and 3:1:0.2, they both  
268 overlap with the distribution of molecules from the sample produced with a H<sub>2</sub>O:CH<sub>3</sub>OH:NH<sub>3</sub>  
269 ratio of 3:1:1 as shown in Figure 3.

270



271

272 **Figure 3: Superposition of the ternary space diagrams of the molecules detected in the sample**  
273 **produced with H<sub>2</sub>O:CH<sub>3</sub>OH:NH<sub>3</sub> ratios of 3:1:1 (black dots) compared to the one detected in the 3:1:5**  
274 **(blue circles) and 3:1:0.2 (red circles) samples. Black, blue and red stars indicate the position of the**  
275 **initial ices on the ternary diagrams, with a ratio H<sub>2</sub>O:CH<sub>3</sub>OH:NH<sub>3</sub> of 3:1:1, the 3:1:5 and the 3:1:0.2**  
276 **respectively.**

277 As visible in this figure, a major fraction of the molecules detected in the 3:1:1 sample are  
278 indeed present either in the 3:1:5 or in the 3:1:0.2 sample. This implies that although the  
279 chemistry leading to the formation of the organic residue can be strongly driven in  
280 distinguishable pathways depending on the ammonia content, the 3:1:1 sample represents an  
281 intermediate case with both pathways starting to emerge (however, both pathways  
282 incomplete in the 3:1:1 sample as the most extreme points of the distribution - high nitrogen  
283 and/or low carbon and/or high oxygen contents - are only populated by the 3:1:0.2 and 3:1:5  
284 samples). This can be confirmed also in the mid-infrared signature of the residue (see spectra  
285 in Fresneau et al. 2017), where the absorption bands in the  $1000\text{-}1700\text{ cm}^{-1}$  wavenumber  
286 range ( $5.9\text{--}10\text{ }\mu\text{m}$ ) of the 3:1:1 residue correspond to the bands detected either in the 3:1:0.2  
287 or the 3:1:5 samples.

### 288 3.1.2. Ammonia and water competition

289 Fresneau et al. 2017 reported that the *average* composition of samples produced with  
290  $\text{H}_2\text{O}:\text{CH}_3\text{OH}:\text{NH}_3$  ratios of 3:1:5 and 10:1:1 were surprisingly similar and confirmed the results  
291 of Henderson and Gudipati 2015 that “*an increase of water or ammonia in the initial ice leads*  
292 *to the same effect: a higher incorporation of nitrogen in the residue*”. This first order similarity  
293 between the residues formed from water and ammonia rich mixtures can be confirmed by  
294 their highly similar infrared signatures (Fresneau et al. 2017) and strong correlations in  
295 modified van Krevelen and ternary space diagrams as visible in Figure SI 2 and Figure SI 3. In  
296 this work we investigate this phenomenon further by comparing, at a molecular level, the two  
297 samples respectively enriched in water and ammonia using the aromaticity criteria  
298 classification (Yassine et al. 2014, Danger et al. 2016).

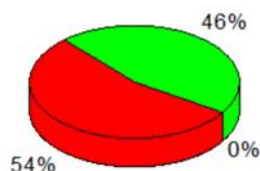
299 Figure 4 a) and b) present the division of different classes of molecules respectively in the  
300 ammonia rich (3:1:5) and water rich (10:1:1) samples. Each molecule detected in these  
301 samples was classified amongst three categories depending on its aromaticity equivalent.  
302 Molecules for which  $0 < X_c < 2.5$  or a double bond equivalent (DBE)  $< 4$  are classified as having  
303 an aliphatic structure with a few unsaturation carried by heteroatoms, molecules for which  
304  $2.5 < X_c < 2.7$  are classified as aromatic based structures and finally molecules with a  $X_c$  higher  
305 than 2.7 are considered to be condensed aromatics. For more information, the histogram of  
306 the complete distribution for all samples is given in Figure SI 1.

a) Ammonia Rich

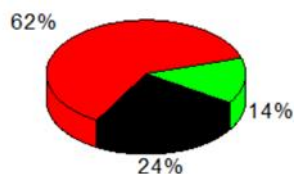
$\text{H}_2\text{O}:\text{CH}_3\text{OH}:\text{NH}_3$

3:1:5

CHN group

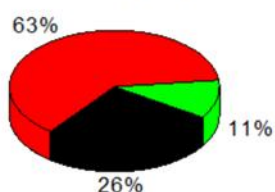


Whole distribution



Aliphatic  $X_c < 2.5$   
 Aromatic  $2.5 < X_c < 2.7$   
 Condensed aromatic  $X_c > 2.7$

CHNO group

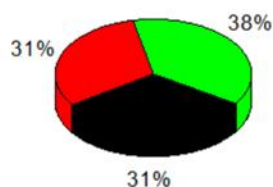


b) Water Rich

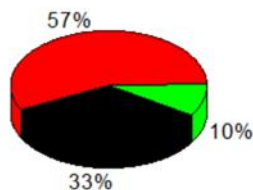
$\text{H}_2\text{O}:\text{CH}_3\text{OH}:\text{NH}_3$

10:1:1

CHN group

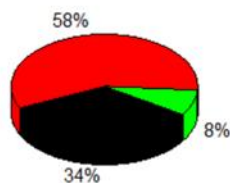


Whole distribution



Aliphatic  $X_c < 2.5$   
 Aromatic  $2.5 < X_c < 2.7$   
 Condensed aromatic  $X_c > 2.7$

CHNO group



307

308 **Figure 4 : a) Repartition of the molecules detected in the Ammonia rich  $\text{H}_2\text{O}:\text{CH}_3\text{OH}:\text{NH}_3$  3:1:5 sample**  
 309 **depending on their level of unsaturation based on the evolution of the aromaticity equivalent ( $X_c$ )**  
 310 **for the totality of the molecules detected in the sample (whole distribution, 711 molecules, top**  
 311 **chart), the molecules containing C,H,N and O atoms (CHNO group, 652 molecules, bottom chart) and**  
 312 **the molecules solely containing C, H and N atoms (CHN group, 59 molecules, left chart). No molecules**  
 313 **solely comprised of only C, H and O were identified. b) : Repartition of the molecules detected in the**  
 314 **water rich  $\text{H}_2\text{O}:\text{CH}_3\text{OH}:\text{NH}_3$  10:1:1 sample depending on their level of unsaturation based on the**  
 315 **evolution of the aromaticity equivalent ( $X_c$ ) for the totality of the molecules detected in the sample**  
 316 **(whole distribution, 831 molecules, top chart), the molecules containing C,H,N and O atoms (CHNO**  
 317 **group, 775 molecules, bottom chart) and the molecules solely containing C, H and N atoms (CHN**  
 318 **group, 56 molecules, left chart). No molecules solely comprised of only C, H and O were identified.**  
 319 **The fraction of molecules classified as aliphatic is shown in black, red represent the fraction classified**

320 as aromatic and green the fraction considered to be condensed aromatic molecules. The percentage  
321 corresponds to the one of the molecules classified according to a given aromaticity relatively to the  
322 entire distribution. Given the number of classified molecules and their variability in the replicates,  
323 we can make a conservative estimate of  $\pm 10\%$  as the  $2\sigma$  uncertainties associated with this  
324 classification for the CHN groups. Uncertainties on the CHNO and whole distributions percentages  
325 are much lower.

326 When looking at the whole distribution (top charts in Figure 4a and b), corresponding to the  
327 molecules identified in the ammonia rich and water rich samples respectively, the major  
328 fraction of the molecules detected in these samples fits into the aromatic category (roughly  
329 60%). The second most predominant class corresponds to the aliphatic molecules (24% and  
330 33% respectively for the 3:1:5 and 10:1:1: sample) and the least present group is the one  
331 comprised of condensed aromatics (14% and 10% respectively). Given the associated error  
332 bars of these distributions, we can conclude that, taken as a whole, both samples have a  
333 practically identical molecular content as previously observed. This is actually driven by the  
334 similarity of the CHNO groups (bottom charts) of 3:1:5 and 10:1:1 that comprise  $\sim 90\%$  of the  
335 molecules detected in these samples.

336 Differences between the ammonia and the water driven residues become noticeable when it  
337 comes to the molecules containing solely carbon, hydrogen and nitrogen atoms, the CHN  
338 group (left charts in Figure 4a and 4b). However, these effects are visible on a minor fraction  
339 of the total attributed peaks (59 and 56 molecules in the CHN group for 3:1:5 and 10:1:1  
340 samples respectively), potentially rendering the statistics poorly representative of the samples  
341 and the following paragraph discussion presents only hypotheses that would require further  
342 investigated in the future: for the sample produced from an ammonia rich ice, the CHN group  
343 does not contain any aliphatic molecules. This indicates that the ammonia could tend to drive  
344 the molecular growth leading to the formation of the CHN fraction toward aromatization,  
345 probably due to the likelihood of nitrogen atom inclusion in aromatic structures. On the other  
346 hand, the CHN fraction of the sample produced from water rich ice has the highest aliphatic

347 content of all the samples investigated in this work (see Figure SI 4 and Figure SI 5 for the other  
348 samples distributions). This effect does not appear to be correlated with the length of the  
349 chains as both distributions have a similar average  $m/z$  (266.04 for the ammonia rich sample  
350 and 267.02 for the water rich sample). For further discussion on the aromaticity of the  
351 residues, readers can direct themselves to Fresneau et al. 2017 and its Figure 5 presenting the  
352 DBE vs N/C ratio in both positive and negative mode of the 3:1:1 sample.

### 353 3.1.3. Effects on the ice reactivity

354 The chemistry driving the residue formation is largely dependent on radical chemistry at low  
355 temperature (77K) (Danger et al., 2013). During the UV irradiation, the initial molecules in the  
356 ices are photo-activated leading to the formation of radicals. In case of H<sub>2</sub>O, CH<sub>3</sub>OH and NH<sub>3</sub>  
357 ices, H<sup>•</sup> and OH<sup>•</sup> are formed from H<sub>2</sub>O, H<sup>•</sup> and NH<sub>2</sub><sup>•</sup> for NH<sub>3</sub> and various radicals from CH<sub>3</sub>OH  
358 such as CH<sub>3</sub>O<sup>•</sup>, HCO<sup>•</sup>, CH<sub>2</sub>OH<sup>•</sup>, CH<sub>3</sub><sup>•</sup> and OH<sup>•</sup>. Therefore, the radical recombination leading to  
359 the first molecules at low temperature is highly impacted by the initial ice composition.  
360 Furthermore, this reactivity probably occurs concomitantly to the evolution of morphological  
361 and physical properties of organic residues, as observed by Piani et al. (2017). In the case of  
362 ices rich in H<sub>2</sub>O, water photochemistry increases the amount of radical hydrogen (H<sup>•</sup>), which  
363 rapidly migrates through the ice at 77K, potentially increasing a rapid recombination with  
364 other radicals. This recombination would be enhanced depending on the temperature, since  
365 Tachibana et al., (2017) observed a liquid-like behavior at 50-150 K in such ice. This  
366 observation would imply a higher radical diffusion in UV-irradiated ice leading to an effective  
367 formation of organic molecules. This would imply a fast-paced saturation of the alkyl chains  
368 during the molecular growth of the residue. Furthermore, H<sub>2</sub>O can act as a diluting agent  
369 spatially separating the different radicals at low temperature and limiting their direct

370 recombination for those that do not migrate at this temperature. Therefore, a higher content  
371 of H<sub>2</sub>O in the initial ice could limit the incorporation of nitrogen on the molecular skeleton,  
372 which is not the case when NH<sub>3</sub> is dominant in the initial ice. This effect is actually visible in  
373 the higher N/C ratio detected in the ammonia rich sample (1.8 on average for molecules of  
374 the CHN group) versus the one of the water rich sample (0.8 on average for the CHN group).  
375 For the ammonia rich mixture, nitrogen radicals quickly saturate carbon-bearing radicals,  
376 implying a fast incorporation of nitrogen atoms into the molecular skeletons.

377 These results clearly demonstrate that nitrogen plays an important role in the chemistry of  
378 the residue formation. Next to carbon, it drives the chemistry and directly impacts the global  
379 molecular skeleton of the residues formed. At high amounts of NH<sub>3</sub> in the initial ice, nitrogen  
380 competes with carbon, implying the formation of molecules-bearing skeletons mixing nitrogen  
381 and carbon. This leads to the formation of higher unsaturated structures such as nitrogen  
382 heterocycles. Interestingly, as observed for residues produced from a H<sub>2</sub>O:CH<sub>3</sub>OH:NH<sub>3</sub> 3:1:1,  
383 with the same amount of C vs. N in the initial ice, a well-balanced chemistry is driven by  
384 nitrogen and carbon leading to a molecular diversity fading of the dichotomy observed  
385 between 3:1:5 and 3:1:0.2 ices. Nitrogen is thus not only a heteroatom allowing the formation  
386 of specific chemical functions such as amines, nitriles or amides. Nitrogen incorporation also  
387 probably enhances the formation of polar structure in the residue, reacting easily with radicals  
388 when the ice is warmed. Nitrogen is thus an important reactant impacting the chemistry  
389 driving the residues formation, at the difference of oxygen as discussed in the next section. It  
390 is also interesting to note that without NH<sub>3</sub> in the mixture almost no residue is obtained.

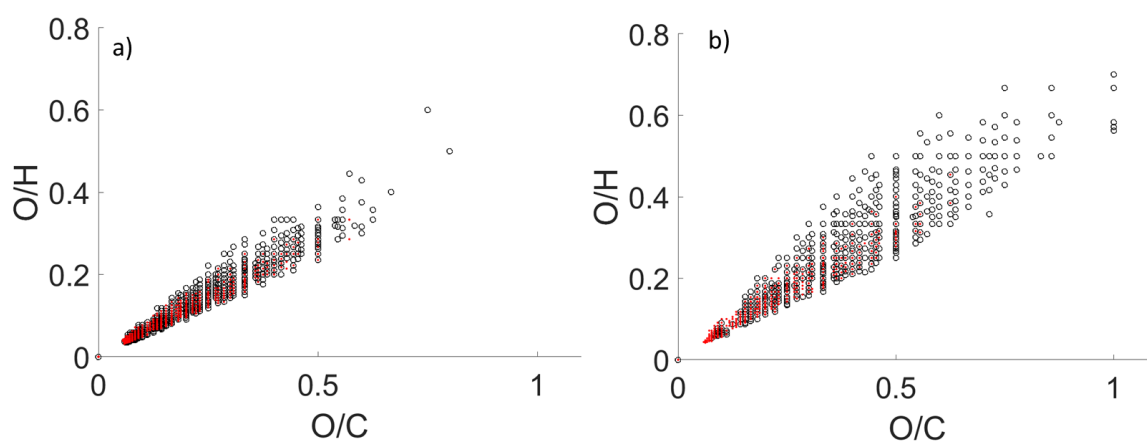
391 Furthermore, the observed reactivity in the residue formation is directly correlated to  
392 molecules detected in the gas phase while the ice is warmed up to 300 K. Abou Mrad et al.,  
393 2017 have shown that CHO molecule abundances in the gas phase are highly influenced by

394 the presence of ammonia in the initial ice. Indeed, the presence of ammonia reduces the  
395 amount of aldehyde observed in the gas phase by recombination of the aldehyde precursor  
396 radicals with radicals produced by  $\text{NH}_3$  photodestruction. The same behavior between radicals  
397 is observed for ethers. Therefore, at least in the laboratory, a direct relation can be drawn  
398 between the residue composition and the molecular abundances in the gas phase. Such  
399 investigation is beyond the scope of this manuscript, but the monitoring of the gas phase  
400 during the residue irradiation could help identifying processes at act during this phase.

### 401 3.2. Residue irradiation

#### 402 3.2.1. Evidence of molecular decarboxylation

403 To visualize the effect of sample over-irradiation at the molecular level we used a modified  
404 van Krevelen representation as presented in Figures 5, SI 1 and SI 2. Black circles represent  
405 the molecules detected in the sample before over-irradiation in their O/C vs O/H (Figure 5),  
406 H/C vs O/H (Figure SI 6) and H/C vs O/C (Figure SI 7) parameter spaces. Green dots represent  
407 the molecules detected in the sample after over-irradiation.



408

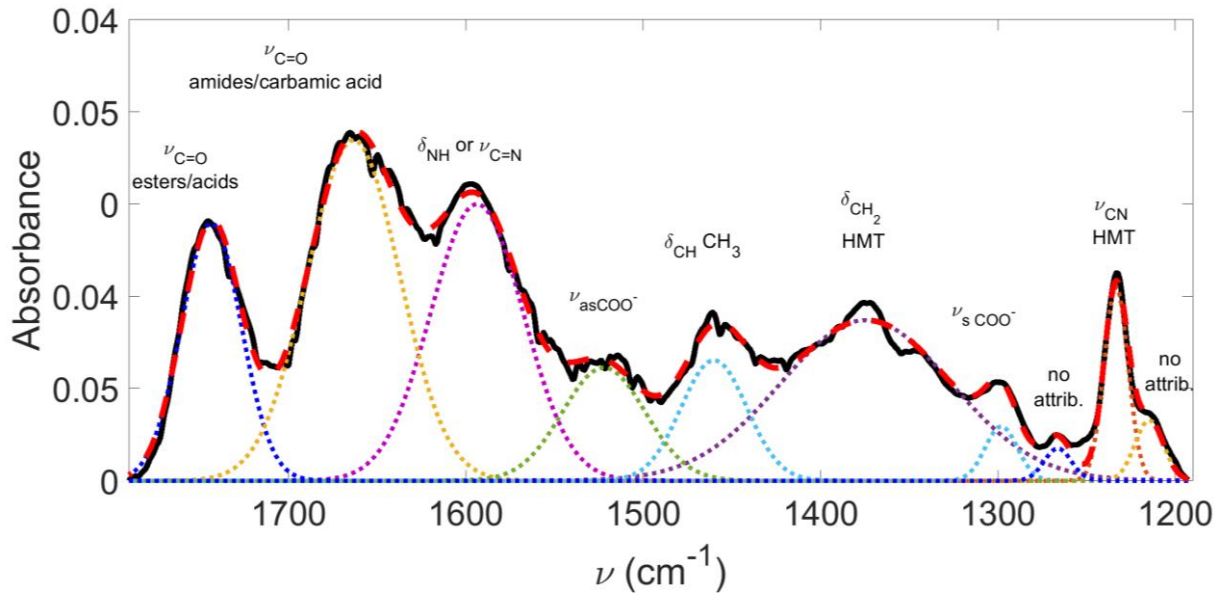
409 **Figure 5: O/C vs O/H modified van Krevelen diagram of the molecules detected in the sample in**  
410 **positive (a) and negative (b) ionization mode before (black circles) and after (green dots) the sample**  
411 **irradiation. See Figures SI 6 and SI 7 for the O/H vs. H/C and H/C vs. O/C representation.**

412 From these visualizations, one can see that a substantial fraction of the molecules initially  
413 present in the soluble fraction of the 3:1:1 sample are not detectable anymore after over-  
414 irradiation of the sample. These molecules degraded during irradiation do have the following  
415 compositional parameters: (i) an oxygen to hydrogen ratio greater than 0.3 which is  
416 significantly higher than the O/H ratio of most of the molecules detected in the over-irradiated  
417 sample; (ii) an oxygen to carbon ratio greater than 0.4; and (iii) a hydrogen to carbon ratio  
418 lower than 1.7. We can reasonably exclude this being solely due to a detection effect (such as  
419 an intensity threshold) since (1) this effect is visible in all replicates of the experiments and (2)  
420 these molecules are significantly located in the same area of the parameter space and not  
421 randomly dispersed in Figures 5, SI 1 and SI 2.

422 The loss of molecules upon over-irradiation also corresponds to molecules detected in the  
423 negative ionization mode. This implies that chemical functions bearing acidic hydrogen such  
424 as carboxylic acids are strongly affected (Holčapek et al., 2007; Krueve et al., 2014).  
425 Concomitantly to this loss in the over-irradiated samples, new molecules are observed, mainly  
426 in the negative ionization mode, with lower O/H and O/C ratios (see Figure SI 7). The residue  
427 over-irradiation seems to induce a decarboxylation process, clearly visible in the negative  
428 mode, which presents a disappearance of molecules at high O/C and O/H in total concordance  
429 to a loss of COOR (R: H or alkyl) groups, and in counterpart, the appearance of new molecules  
430 at low O/C and O/H. However, the whole mechanism is not entirely observable by HRMS  
431 analyses, since a part of the molecules modified by the over-irradiation phase is actually  
432 insoluble (de Marcellus et al., 2017) and thus not taken into account in this type of analysis.

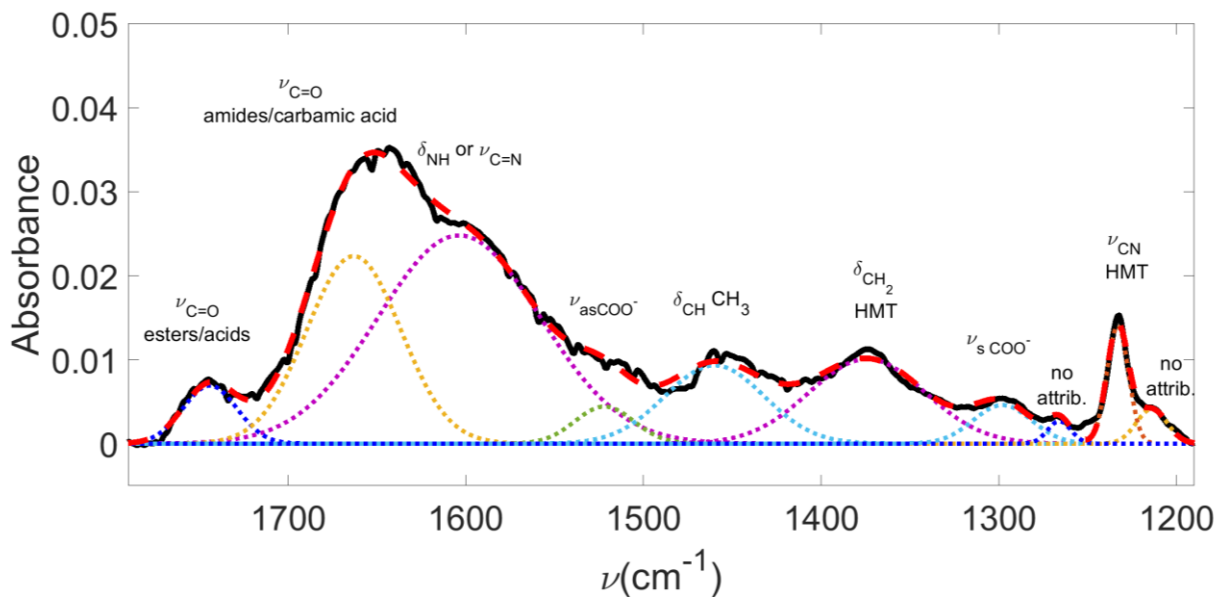
433 This decarboxylation was thus confirmed by the infrared absorption spectra of the residue  
434 before and after irradiation. These spectra are presented in Figures 6 and 7 together with their

435 Gaussian deconvolution. Bands attributions and positions are the ones described in Fresneau  
 436 et al. 2017.



437

438 **Figure 6: Gaussian deconvolution after baseline subtraction of the 1200-1850  $\text{cm}^{-1}$  region of the IR**  
 439 **absorption spectrum of the residue produced from 3:1:1 ices before its irradiation. The measured**  
 440 **spectrum is in full black, the deconvoluted Gaussians in dotted color lines and the dashed red line**  
 441 **corresponds to the reconstructed fit after deconvolution. For the Gaussian fit, band positions were**  
 442 **taken from Fresneau et al. 2017 and their intensities and HWHM were fitted iteratively using Fityk**  
 443 **software.**



444

445 **Figure 7: Gaussian deconvolution after baseline subtraction of the 1200-1850  $\text{cm}^{-1}$  region of the IR**  
 446 **absorption spectrum of the residue produced from 3:1:1 ices after its irradiation. The measured**  
 447 **spectrum is in full black, the deconvoluted Gaussians in dotted color lines and the dashed red line**

448 corresponds to the reconstructed fit after deconvolution. For the Gaussian fit, band positions were  
449 taken from Fresneau et al. 2017 and their intensities and HWHM were fitted iteratively using Fityk  
450 software.

451

452 As visible in these figures, the C=O stretch in esters or acids (blue Gaussian curves) is strongly  
453 depleted by the irradiation of the sample compared to C=O stretch in amides (orange Gaussian  
454 curves). As a counterpart, the NH bendings or C=N bands appear stronger in the over-  
455 irradiated sample.

456 Together with the HRMS analyses we can thus conclude that the residue over-irradiation  
457 induces a strong decarboxylation process. This result would imply a fast decay of carboxylic  
458 functions in the protosolar organic matter analog upon UV irradiation. Regarding residue  
459 irradiation, in addition to the chemical changes we investigate in our work, it should also be  
460 noted that Piani et al. (2017) have also reported significant evolution of morphological and  
461 physical properties of organic residues formed from the evolution of H<sub>2</sub>O-CH<sub>3</sub>OH-NH<sub>3</sub> ices due  
462 to UV irradiation.

463 3.2.2. Possible implications of this decarboxylation process on the –COOR molecules  
464 in meteorites

465 Fresneau et al. 2017 have defined an  $\alpha$  parameter as  $\alpha = \frac{A_{1745\text{ cm}^{-1}}}{A_{1665\text{ cm}^{-1}}}$  where  $A_{1745\text{ cm}^{-1}}$  is the  
466 area of the  $\nu_{\text{C=O}}$  band of ester or acids and  $A_{1665\text{ cm}^{-1}}$  is the area of the  $\nu_{\text{C=O}}$  band of amide or  
467 carbamic acid. Using the area of the deconvoluted Gaussian presented in Figure 6 and  
468 **Figure 7**, we can retrieve the value of  $\alpha$  to be 0.54 in the residue before irradiation, while it  
469 plummets to 0.09 after the residue irradiation. Given the 48 hours of the over-irradiation of  
470 our sample and that our lamp has a fluence of  $2 \times 10^{14}$  photons.cm<sup>-2</sup>.s<sup>-1</sup>, the total dose

471 deposited in our sample is of  $3.5 \times 10^{19}$  photons.cm<sup>-2</sup>. The experimental conditions used here  
472 can be compared with the model developed by Ciesla and Sandford, 2012, which describes  
473 the exposure of ice grains to the UV flux during their dynamical evolution within the protosolar  
474 nebula (PSN). In their nominal model, these authors find that a typical dose for particles with  
475 1  $\mu\text{m}$  radii is about  $5 \times 10^{12}$  photons after 1 Myrs of radial and vertical transport within the  
476 disk, and assuming a nominal interstellar UV flux of  $10^8$  photons cm<sup>-2</sup>.s<sup>-1</sup> (Habing, 1968). This  
477 would give a dose for such particles of  $1.6 \times 10^{20}$  photons cm<sup>-2</sup> in 1 Myrs. In comparison, the  
478 total dose from our experiment of  $3.5 \times 10^{19}$  photons.cm<sup>-2</sup> would represent  $\sim 220$  kyrs of the  
479 evolution of Ciesla and Sandford (2012)'s PSN model for such particles.

480 Our results show that these 220 kyrs would be enough to induce a dramatic decrease in the  
481 -COOR or -COOH functional group of the organic matter in the grains. If organic rich particles  
482 indeed spent  $\sim 1$  Myr in the PSN, they would be completely depleted in such functional groups.  
483 This conclusion is not in agreement with measurement performed on chondritic meteorites,  
484 where carboxylic acids are a major component of the soluble organic matter. For example, in  
485 the Murchison meteorite (CM2), the total abundance of carboxylic acids has been estimated  
486 to be around  $330 \mu\text{g g}^{-1}$ , roughly 40% of the identified organic content and more than any  
487 other organic groups besides the macromolecular structure (Lawless and Yuen, 1979;  
488 Pizzarello and Shock, 2010b; Sephton, 2002; Yuen et al., 1984).

489 The reader should keep in mind that our results are based on only one kinetic irradiation point  
490 (48h in the laboratory – 220 kyrs in the PSN) and that further experiments should be dedicated  
491 to the study of the kinetics of carboxylic functions degradation. However, our results suggest  
492 a fast decay of the carboxylic acids and carboxylic esters functional groups upon UV

493 irradiation. This fast decay could be in contradiction with their high abundances in CM. This  
494 may have at least three different explanations, and possibly a combination of them;

495 1- The organic matter could be shielded in the protosolar nebula either by silicates or self-  
496 shielded. This phenomenon may be strong enough to, at least partially, shield the carboxylic  
497 function until their inclusion in CM parent bodies (Greenberg, 1993; Herbst, 2001). However  
498 self-shielding by organic matter in only 1  $\mu\text{m}$  size grains as proposed by Ciesla and Stanford  
499 2012 seems unlikely.

500 2- The timescale on which the organic residue would be irradiated may be much shorter than  
501 the irradiation time of  $\sim 220$  kyrs investigated in this paper, due for example to shorter lifetime  
502 of the PSN or more effective convection in the disk. The advantage of irradiation timescales  
503 much shorter than 1 Myrs is that they are consistent with dynamical scenarios predicting the  
504 growth of grains and their decoupling from gas within fifty thousands of years of the disk  
505 evolution (Weidenschilling and Cuzzi, 1993). It also should be noted that a similar dose could  
506 be attained in much shorter irradiation timescales in the PSN if one assumes an enhanced  
507 interstellar UV flux. This interstellar flux can be higher by a factor of  $10^3$  compared to the  
508 nominal one, depending on the possible presence of nearby stars at that time as supported  
509 by the presence of certain radio elements in meteorites (Adams et al., 2006; Gounelle and  
510 Meynet, 2012).

511 3- The carboxylic functions detected in CM meteorites may just simply not be inherited from  
512 the organic matter formed in the ISM and altered solely by photoprocesses within the edge of  
513 the protosolar nebula as described in Ciesla and Sandford (2012). Instead such material may  
514 have been, at least partially, reprocessed during later stages of the solar system formation. A  
515 potential pathway for the reprocessing of carboxylic acid could be via the hydrolysis of nitriles

516 functions by aqueous alteration in meteorites parent body (Cronin and Chang, 1993). In regard  
517 to these hypotheses it has to be noted that CM meteorites aliphatic hydrocarbons have a  
518 consistently lighter  $\delta^{13}\text{C}$  compared to carboxylic groups, pointing either toward an isotopically  
519 selective process in the transformation of these materials from ISM to CM parent bodies, or  
520 toward the fact that the carboxylic and aliphatic groups of the SOM are derived from  
521 isotopically-distinct reservoirs (Aponte et al., 2019; Sephton, 2002; Yuen et al., 1984).  
522 However, studies performed on the Insoluble Organic Matter of CM meteorites have shown  
523 that the carboxylic group only represents a minor fraction of this material and is narrowly  
524 affected by aqueous alteration (Cody and Alexander, 2005; Orthous-Daunay et al., 2013).  
525 Aponte et al., (2019) also extensively discussed the carbon isotopic fractionation of carboxylic  
526 acid in chondrites. They found decreasing concentrations of monocarboxylic acid with  
527 increasing processing (aqueous and thermal) and that the least oxidized CR chondrites contain  
528 higher concentration of carboxylic acids than CM, CO, CV and CK chondrites suggesting that if  
529 formed in parent bodies *“The accretion of aliphatic precursors of monocarboxylic acids was  
530 not homogeneous throughout different parent bodies, or that the abundance of  
531 monocarboxylic acids was mostly affected by parent body processes”*. Again we emphasize on  
532 the need for further experimental data on the kinetics of carboxylic function degradation in  
533 the PSN until the accretion in parent bodies.

#### 534 **4. Conclusions**

535 We used laboratory experiments to obtain deeper information on the reactivity occurring  
536 during the processing of icy grains. Ice analogs are submitted to processes endured by ices  
537 when they evolve within a proto-planetary disk, meaning in our experimental conditions UV  
538 irradiation at Lyman  $\alpha$  and heating. Organic residues obtained in vacuum at 300 K are then

539 analyzed by very high-resolution mass spectrometry (HRMS) using a LTQ-XL-orbitrap. HRMS  
540 analyses provide invaluable information on the molecular content of each residue. Data  
541 obtained allow comparing the residue evolution for residues formed from different ice  
542 compositions (variability of H<sub>2</sub>O and NH<sub>3</sub> in the initial ice). We particularly show that nitrogen  
543 atoms take an important role in the reactivity by competing with the carbon, the resulting  
544 composition of residues depending on the initial amount of ammonia in the ice. Higher relative  
545 amounts of ammonia in the ices for a same ratio H<sub>2</sub>O/CH<sub>3</sub>OH leads to residue enrichment in  
546 nitrogen and to the formation of higher unsaturated structures (nitrogen in cycles). It was  
547 previously shown with FT-IR analyses and elemental analyses by HRMS that a higher amount  
548 of water in the initial ice also leads to an enrichment of residues in nitrogen. We confirm these  
549 results and by going deeper in the molecular content of the residues, we emphasize that this  
550 similarity is only the tip of the iceberg. In fact, similarities between residues coming from  
551 nitrogen or water rich ices are due to the prevalence of CHNO molecules forming residues that  
552 are indeed similar. However, our present investigation shows that a difference exists in  
553 molecules bearing only CHN atoms. In ammonia rich ices, this group is only unsaturated while  
554 in water rich ones, it is mainly saturated. Here again, the reactivity of ammonia and water  
555 explains these results, since ammonia drives the residue formation toward aromatization of  
556 CHN molecules while water rich ice tends to form aliphatic rich residues. Finally, we  
557 demonstrate that residue over-irradiation at 300 K leads to a quick decarboxylation of some  
558 of the molecules. This result could have an important impact in our understanding of  
559 protosolar nebula timescales and of the molecular processes leading to the organic matter  
560 detected in meteorites.

561

562 **Acknowledgments**

563 The authors wish to thank P.A. Girardi for proof-reading the language of this manuscript. T.G.  
564 thanks CNES for a postdoctoral grant during part of this work. G.D. thanks the ANR support  
565 from the grant RAHIIA\_SSOM (ANR-16-CE29-0015), the CNES from its exobiology program, as  
566 well as the CNRS from the PCMI and PNP programs. L.L.S.H. thanks the French national space  
567 agency (CNES) for its constant support in the MICMOC experiment at the origin of these  
568 residues.

569 **References**

- 570 Abou Mrad, N., Duvernay, F., Isnard, R., Chiavassa, T., Danger, G., 2017. The Gaseous Phase  
571 as a Probe of the Astrophysical Solid Phase Chemistry. *Astrophys. J.* 846, 124.  
572 <https://doi.org/10.3847/1538-4357/aa7cf0>
- 573 Adams, F.C., Proszkow, E.M., Fatuzzo, M., Myers, P.C., 2006. Early Evolution of Stellar Groups  
574 and Clusters: Environmental Effects on Forming Planetary Systems. *Astrophys. J.* 641,  
575 504–525. <https://doi.org/10.1086/500393>
- 576 Aponte, J.C., Woodward, H.K., Abreu, N.M., Elsila, J.E., Dworkin, J.P., 2019. Molecular  
577 distribution, <sup>13</sup>C-isotope, and enantiomeric compositions of carbonaceous chondrite  
578 monocarboxylic acids. *Meteorit. Planet. Sci.* 54, 415–430.  
579 <https://doi.org/10.1111/maps.13216>
- 580 Bernstein, D.I., Sandford, S.A., Allamandola, L.J., Chang, S., Bernstein, M., Scharberg, M.A.,  
581 1995. Organic compounds produced by photolysis of realistic interstellar and cometary  
582 ice analogs containing methanol. *Astrophys. J.* 454, 327–344.
- 583 Bernstein, M.P., Sandford, S.A., Allamandola, L.J., Chang, S., Scharberg, M.A., 1995. Organic

584 Compounds Produced by Photolysis of Realistic Interstellar and Cometary Ice Analogs  
585 Containing Methanol. *Astrophys. J.* 454, 327. <https://doi.org/10.1086/176485>

586 Boogert, A.C.A., Pontoppidan, K.M., Knez, C., Lahuis, F., Kessler-Silacci, J., van Dishoeck, E.F.,  
587 Blake, G.A., Augereau, J. -C., Bisschop, S.E., Bottinelli, S., Brooke, T.Y., Brown, J., Crapsi,  
588 A., Evans II, N.J., Fraser, H.J., Geers, V., Huard, T.L., Jørgensen, J.K., Öberg, K.I., Allen,  
589 L.E., Harvey, P.M., Koerner, D.W., Mundy, L.G., Padgett, D.L., Sargent, A.I., Stapelfeldt,  
590 K.R., 2008. The c2d *Spitzer* Spectroscopic Survey of Ices around Low-Mass Young Stellar  
591 Objects. I. H<sub>2</sub>O and the 5–8 μm Bands<sup>1,2</sup>. *Astrophys. J.* 678, 985–1004.  
592 <https://doi.org/10.1086/533425>

593 Briggs, R., Ertem, G., Ferris, J.P., Greenberg, J.M., McCain, P.J., Mendoza-Gomez, C.X.,  
594 Schutte, W., 1992. Comet Halley as an aggregate of interstellar dust and further  
595 evidence for the photochemical formation of organics in the interstellar medium. *Orig.*  
596 *Life Evol. Biosph.* 22, 287–307. <https://doi.org/10.1007/BF01810858>

597 Burton, A.S., Glavin, D.P., Elsila, J.E., Dworkin, J.P., Jenniskens, P., Yin, Q.-Z., 2014. The amino  
598 acid composition of the Sutter’s Mill CM2 carbonaceous chondrite. *Meteorit. Planet.*  
599 *Sci.* 49, 2074–2086. <https://doi.org/10.1111/maps.12281>

600 Callahan, M.P., Martin, M.G., Burton, A.S., Glavin, D.P., Dworkin, J.P., 2014. Amino acid  
601 analysis in micrograms of meteorite sample by nanoliquid chromatography–high-  
602 resolution mass spectrometry. *J. Chromatogr. A* 1332, 30–34.  
603 <https://doi.org/10.1016/j.chroma.2014.01.032>

604 Ciesla, F.J., Sandford, S.A., 2012. Organic Synthesis via Irradiation and Warming of Ice Grains  
605 in the Solar Nebula. *Science* (80-. ). 336.

606 Clark, R.N., Carlson, R., Grundy, W., Noll, K., 2013. Observed Ices in the Solar System.  
607 Springer, New York, NY, pp. 3–46. [https://doi.org/10.1007/978-1-4614-3076-6\\_1](https://doi.org/10.1007/978-1-4614-3076-6_1)

608 Cody, G.D., Alexander, C.M.O. 'D., 2005. NMR studies of chemical structural variation of  
609 insoluble organic matter from different carbonaceous chondrite groups. *Geochim.*  
610 *Cosmochim. Acta* 69, 1085–1097. <https://doi.org/10.1016/J.GCA.2004.08.031>

611 Cooper, G., Kimmich, N., Belisle, W., Sarinana, J., Brabham, K., Garrel, L., 2001. Carbonaceous  
612 meteorites as a source of sugar-related organic compounds for the early Earth. *Nature*  
613 414, 879–883. <https://doi.org/10.1038/414879a>

614 Cronin, J.R., Chang, S., 1993. Organic Matter in Meteorites: Molecular and Isotopic Analyses  
615 of the Murchison Meteorite, in: *The Chemistry of Life's Origins*. Springer Netherlands,  
616 Dordrecht, pp. 209–258. [https://doi.org/10.1007/978-94-011-1936-8\\_9](https://doi.org/10.1007/978-94-011-1936-8_9)

617 Cronin, J.R., Moore, C.B., 1971. Amino Acid Analyses of the Murchison, Murray, and Allende  
618 Carbonaceous Chondrites. *Science* (80-. ). 172, 1327–1329.  
619 <https://doi.org/10.1126/science.172.3990.1327>

620 Danger, G., Fresneau, A., Abou Mrad, N., de Marcellus, P., Orthous-Daunay, F.-R., Duvernay,  
621 F., Vuitton, V., Le Sergeant d'Hendecourt, L., Thissen, R., Chiavassa, T., 2016. Insight into  
622 the molecular composition of laboratory organic residues produced from  
623 interstellar/pre-cometary ice analogues using very high resolution mass spectrometry.  
624 *Geochim. Cosmochim. Acta* 189, 184–196. <https://doi.org/10.1016/j.gca.2016.06.014>

625 Danger, G., Orthous-Daunay, F.-R., de Marcellus, P., Modica, P., Vuitton, V., Duvernay, F.,  
626 Flandinet, L., Le Sergeant d'Hendecourt, L., Thissen, R., Chiavassa, T., 2013.  
627 Characterization of laboratory analogs of interstellar/cometary organic residues using

628 very high resolution mass spectrometry. *Geochim. Cosmochim. Acta* 118, 184–201.  
629 <https://doi.org/10.1016/j.gca.2013.05.015>

630 de Marcellus, P., Fresneau, A., Brunetto, R., Danger, G., Duvernay, F., Meinert, C.,  
631 Meierhenrich, U.J., Borondics, F., Chiavassa, T., d’Hendecourt, L.L.S., 2017. Photo and  
632 thermochemical evolution of astrophysical ice analogues as a source for soluble and  
633 insoluble organic materials in Solar system minor bodies. *Mon. Not. R. Astron. Soc.*  
634 <https://doi.org/10.1093/mnras/stw2292>

635 de Marcellus, P., Meinert, C., Myrgorodska, I., Nahon, L., Buhse, T., d’Hendecourt, L.L.S.,  
636 Meierhenrich, U.J., 2015. Aldehydes and sugars from evolved precometary ice analogs:  
637 Importance of ices in astrochemical and prebiotic evolution. *Proc. Natl. Acad. Sci.*  
638 <https://doi.org/10.1073/pnas.1418602112>

639 De Sanctis, M.C., Ammannito, E., McSween, H.Y., Raponi, A., Marchi, S., Capaccioni, F.,  
640 Capria, M.T., Carrozzo, F.G., Ciarniello, M., Fonte, S., Formisano, M., Frigeri, A.,  
641 Giardino, M., Longobardo, A., Magni, G., McFadden, L.A., Palomba, E., Pieters, C.M.,  
642 Tosi, F., Zambon, F., Raymond, C.A., Russell, C.T., 2017. Localized aliphatic organic  
643 material on the surface of Ceres. *Science* 355, 719–722.  
644 <https://doi.org/10.1126/science.aaj2305>

645 Gautier, T., Carrasco, N., Schmitz-Afonso, I., Touboul, D., Szopa, C., Buch, A., Pernot, P., 2014.  
646 Nitrogen incorporation in titan’s tholins inferred by high resolution orbitrap mass  
647 spectrometry and gas chromatography-mass spectrometry. *Earth Planet. Sci. Lett.* 404,  
648 33–42. <https://doi.org/10.1016/j.epsl.2014.07.011>

649 Goesmann, F., Rosenbauer, H., Bredehoeft, J.H., Cabane, M., Ehrenfreund, P., Gautier, T.,  
650 Giri, C., Krueger, H., Le Roy, L., MacDermott, A.J., McKenna-Lawlor, S., Meierhenrich,

651 U.J., Munoz Caro, G.M., Raulin, F., Roll, R., Steele, A., Steininger, H., Sternberg, R.,  
652 Szopa, C., Thiemann, W., Ulamec, S., 2015. Organic compounds on comet  
653 67P/Churyumov-Gerasimenko revealed by COSAC mass spectrometry. *Science* (80- ).  
654 <https://doi.org/10.1126/science.aab0689>

655 Gounelle, M., Meynet, G., 2012. Solar system genealogy revealed by extinct short-lived  
656 radionuclides in meteorites. <https://doi.org/10.1051/0004-6361/201219031>

657 Greenberg, J.M., 1993. Physical and Chemical Composition of Comets — From Interstellar  
658 Space to the Earth, in: *The Chemistry of Life's Origins*. Springer Netherlands, Dordrecht,  
659 pp. 195–207. [https://doi.org/10.1007/978-94-011-1936-8\\_8](https://doi.org/10.1007/978-94-011-1936-8_8)

660 Habing, H.J., 1968. The interstellar radiation density between 912 Å and 2400 Å. *Bull. Astron.*  
661 *Institutes Netherlands* 19, 421.

662 Henderson, B.L., Gudipati, M.S., 2015. DIRECT DETECTION OF COMPLEX ORGANIC PRODUCTS  
663 IN ULTRAVIOLET ( $\text{Ly}\alpha$ ) AND ELECTRON-IRRADIATED ASTROPHYSICAL AND COMETARY  
664 ICE ANALOGS USING TWO-STEP LASER ABLATION AND IONIZATION MASS  
665 SPECTROMETRY. *Astrophys. J.* 800, 66. <https://doi.org/10.1088/0004-637X/800/1/66>

666 Herbst, E., 2001. The chemistry of interstellar space. *Chem. Soc. Rev.* 30, 168–176.  
667 <https://doi.org/10.1039/a909040a>

668 Hertkorn, N., Frommberger, M., Witt, M., Koch, B.P., Schmitt-Kopplin, P., Perdue, E.M., 2008.  
669 Natural Organic Matter and the Event Horizon of Mass Spectrometry. *Anal. Chem.* 80,  
670 8908–8919. <https://doi.org/10.1021/ac800464g>

671 Holčapek, M., Volná, K., Vaněrková, D., 2007. Effects of functional groups on the  
672 fragmentation of dyes in electrospray and atmospheric pressure chemical ionization

673 mass spectra. *Dye. Pigment.* 75, 156–165.  
674 <https://doi.org/10.1016/J.DYEPIG.2006.05.040>

675 Howarth, R.J., 1996. Sources for a history of the ternary diagram. *Br. J. Hist. Sci.* 29, 337.  
676 <https://doi.org/10.1017/S000708740003449X>

677 Kim, S., Kramer, R.W., Hatcher, P.G., 2003. Graphical Method for Analysis of Ultrahigh-  
678 Resolution Broadband Mass Spectra of Natural Organic Matter, the Van Krevelen  
679 Diagram. *Anal. Chem.* 75, 5336–5344. <https://doi.org/10.1021/ac034415p>

680 Kruve, A., Kaupmees, K., Liigand, J., Leito, I., 2014. Negative Electrospray Ionization via  
681 Deprotonation: Predicting the Ionization Efficiency. *Anal. Chem.* 86, 4822–4830.  
682 <https://doi.org/10.1021/ac404066v>

683 Lawless, J.G., Yuen, G.U., 1979. Quantification of monocarboxylic acids in the Murchison  
684 carbonaceous meteorite. *Nature* 282, 396–398. <https://doi.org/10.1038/282396a0>

685 Martins, Z., Modica, P., Zanda, B., d’Hendecourt, L.L.S., 2015. The amino acid and  
686 hydrocarbon contents of the Paris meteorite: Insights into the most primitive CM  
687 chondrite. *Meteorit. Planet. Sci.* 50, 926–943. <https://doi.org/10.1111/maps.12442>

688 Meech, K.J., Svoren, J., 2004. Using cometary activity to trace the physical and chemical  
689 evolution of cometary nuclei. *Comets II* 317.

690 Meinert, C., Myrgorodska, I., de Marcellus, P., Buhse, T., Nahon, L., Hoffmann, S. V,  
691 d’Hendecourt, L.L.S., Meierhenrich, U.J., 2016. Ribose and related sugars from  
692 ultraviolet irradiation of interstellar ice analogs. *Science* 352, 208–12.  
693 <https://doi.org/10.1126/science.aad8137>

694 Muñoz Caro, G.M., Schutte, W.A., 2003. UV-photoprocessing of interstellar ice analogs: New

695 infrared spectroscopic results. *Astron. Astrophys.* <https://doi.org/10.1051/0004->  
696 6361:20031408

697 Newton, I., 1704. *Opticks: Or, a treatise of the reflexions, refractions, inflexions and colours*  
698 *of light.* R. Br. Soc. <https://doi.org/10.1007/s13398-014-0173-7.2>

699 Nuevo, M., Meierhenrich, U.J., d’Hendecourt, L., Muñoz Caro, G.M., Dartois, E., Deboffle, D.,  
700 Thiemann, W.H.-P., Bredehöft, J.-H., Nahon, L., 2007. Enantiomeric separation of  
701 complex organic molecules produced from irradiation of interstellar/circumstellar ice  
702 analogs. *Adv. Sp. Res.* 39, 400–404. <https://doi.org/10.1016/j.asr.2005.05.011>

703 Nuevo, M., Milam, S.N., Sandford, S.A., De Gregorio, B.T., Cody, G.D., Kilcoyne, A.L.D., 2011.  
704 XANES analysis of organic residues produced from the UV irradiation of astrophysical  
705 ice analogs. *Adv. Sp. Res.* 48, 1126–1135. <https://doi.org/10.1016/j.asr.2011.05.020>

706 Orthous-Daunay, F.-R., Quirico, E., Beck, P., Brissaud, O., Dartois, E., Pino, T., Schmitt, B.,  
707 2013. Mid-infrared study of the molecular structure variability of insoluble organic  
708 matter from primitive chondrites. *Icarus* 223, 534–543.  
709 <https://doi.org/10.1016/J.ICARUS.2013.01.003>

710 Pernot, P., Carrasco, N., Thissen, R., Schmitz-Afonso, I., 2010. Tholinomics—Chemical  
711 Analysis of Nitrogen-Rich Polymers. *Anal. Chem.* 82, 1371–1380.  
712 <https://doi.org/10.1021/ac902458q>

713 Piani, L., Tachibana, S., Hama, T., Tanaka, H., Endo, Y., Sugawara, I., Dessimoulie, L., Kimura,  
714 Y., Miyake, A., Matsuno, J., Tsuchiyama, A., Fujita, K., Nakatsubo, S., Fukushi, H., Mori,  
715 S., Chigai, T., Yurimoto, H., Kouchi, A., 2017. Evolution of Morphological and Physical  
716 Properties of Laboratory Interstellar Organic Residues with Ultraviolet Irradiation.

717       Astrophys. J. 837, 35. <https://doi.org/10.3847/1538-4357/aa5ca6>

718       Pizzarello, S., Shock, E., 2010a. The organic composition of carbonaceous meteorites: the  
719       evolutionary story ahead of biochemistry. *Cold Spring Harb. Perspect. Biol.* 2, a002105.  
720       <https://doi.org/10.1101/cshperspect.a002105>

721       Pizzarello, S., Shock, E., 2010b. The organic composition of carbonaceous meteorites: the  
722       evolutionary story ahead of biochemistry. *Cold Spring Harb. Perspect. Biol.*  
723       <https://doi.org/10.1101/cshperspect.a002105>

724       Ruf, A., Kanawati, B., Hertkorn, N., Yin, Q.-Z., Moritz, F., Harir, M., Lucio, M., Michalke, B.,  
725       Wimpenny, J., Shilobreeva, S., Bronsky, B., Saraykin, V., Gabelica, Z., Gougeon, R.D.,  
726       Quirico, E., Ralew, S., Jakubowski, T., Haack, H., Gonsior, M., Jenniskens, P., Hinman,  
727       N.W., Schmitt-Kopplin, P., 2017. Previously unknown class of metalorganic compounds  
728       revealed in meteorites. *Proc. Natl. Acad. Sci. U. S. A.* 114, 2819–2824.  
729       <https://doi.org/10.1073/pnas.1616019114>

730       Sephton, M.A., 2002. Organic compounds in carbonaceous meteorites. *Nat. Prod. Rep.* 19,  
731       292–311. <https://doi.org/10.1039/b103775g>

732       Somogyi, Á., Smith, M.A., Vuitton, V., Thissen, R., Komáromi, I., 2012. Chemical ionization in  
733       the atmosphere? A model study on negatively charged “exotic” ions generated from  
734       Titan’s tholins by ultrahigh resolution MS and MS/MS. *Int. J. Mass Spectrom.* 316–318,  
735       157–163. <https://doi.org/10.1016/J.IJMS.2012.02.026>

736       Tachibana, S., Kouchi, A., Hama, T., Oba, Y., Piani, L., Sugawara, I., Endo, Y., Hidaka, H.,  
737       Kimura, Y., Murata, K., Yurimoto, H., Watanabe, N., 2017. Liquid-like behavior of UV-  
738       irradiated interstellar ice analog at low temperatures. *Sci. Adv.* 3, eaao2538.

739 <https://doi.org/10.1126/sciadv.aao2538>

740 van Krevelen, D.W., 1950. Graphical-statistical method for the study of structure and  
741 reaction processes of coal. *Fuel*. <https://doi.org/10.1520/D0850-11.1>

742 Weidenschilling, S.J., Cuzzi, J.N., 1993. Formation of Planetesimals in the Solar Nebula.  
743 *Protostars Planets III* 1031.

744 Wu, Z., Rodgers, R.P., Marshall, A.G., 2004. Two- and Three-Dimensional van Krevelen  
745 Diagrams: A Graphical Analysis Complementary to the Kendrick Mass Plot for Sorting  
746 Elemental Compositions of Complex Organic Mixtures Based on Ultrahigh-Resolution  
747 Broadband Fourier Transform Ion Cyclotron Resonance Mass Measurements. *Anal.*  
748 *Chem.* 76, 2511–2516. <https://doi.org/10.1021/ac0355449>

749 Yassine, M.M., Harir, M., Dabek-Zlotorzynska, E., Schmitt-Kopplin, P., 2014. Structural  
750 characterization of organic aerosol using Fourier transform ion cyclotron resonance  
751 mass spectrometry: Aromaticity equivalent approach. *Rapid Commun. Mass Spectrom.*  
752 28, 2445–2454. <https://doi.org/10.1002/rcm.7038>

753 Yuen, G., Blair, N., Des Marais, D.J., Chang, S., 1984. Carbon isotope composition of low  
754 molecular weight hydrocarbons and monocarboxylic acids from Murchison meteorite.  
755 *Nature* 307, 252–254. <https://doi.org/10.1038/307252a0>

756

757 **Supplementary information**

758 *Attributor Data Processing*

759 The first processing step is to remove the instrument noise by deleting the less intense peaks  
760 until reaching a convex intensity distribution. Radio interference and low level noises are also  
761 reduced by isolating structures of interest for the sample in a mass defect versus exact mass  
762 (MDvEM) space representation as depicted in Danger et al. 2013. This representation is also  
763 used to detect and eliminate the ringing effects, visible as vertical lines in the MDvEM. Once  
764 this is done, the software locates the centroids of each Gaussian peak in the spectra and  
765 reduces each peak to its centroid, greatly reducing the size of the data. The same process is  
766 applied to the blank spectra (*i.e.* same experimental protocol with no sample in the solvent).  
767 Peaks found to be present in the blank spectra are then removed from the sample mass  
768 spectra.

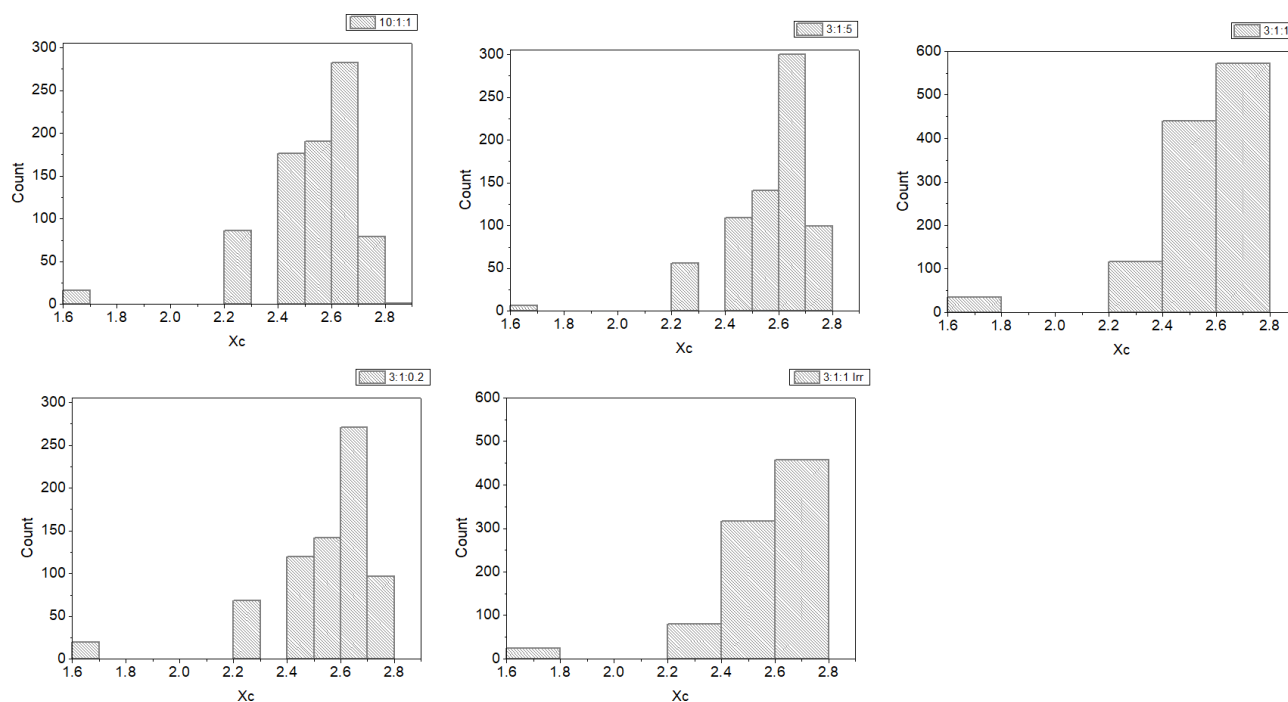
769 The data is then post-calibrated. In *Attributor*, this is done by looking at the distribution of the  
770 mass differences between every single peak of the spectra. Typically, for organic samples, one  
771 expects to find pattern ( $\epsilon$ ) differences at  $\Delta m$  2, 12 or 14, corresponding to a difference in H<sub>2</sub>,  
772 C or CH<sub>2</sub> in the composition of the molecules detected. For a given pattern  $\epsilon$  and in an ideal  
773 case the mass difference between molecules X and X+  $\epsilon$  should not depend of the mass of X.  
774 In reality, when looking at the spectra, we can see multiple pairs of points for which the mass  
775 differences are close to  $\epsilon$  but differ with the masses of X, meaning a bias on the linearity of  
776 the measure. To correct this bias, *Attributor* will check for two correction points corresponding  
777 to *trusted* molecules. These molecules correspond to 2 peaks chosen by *attributor* for which  
778 a molecular formula can be unambiguously attributed. Typically, these correspond to intense  
779 peaks for which 1/ the isotopic patterns with <sup>13</sup>C are clearly identified in the mass spectra and  
780 2/ have univocal possible attribution (the second closest possible attribution would have an  
781 error in ppm far superior to the closest possible attribution). *Attributor* then give a list of  
782 possible attributions for these two trusted molecules that can be checked by the operator

783 before proceeding to the data recalibration. Once these two trusted molecules identified, a  
784 recalibration coefficient is applied to all the peaks in the mass spectra. If needed, this  
785 operation can be repeated until all attributions in the mass spectra are within a 2ppm error  
786 window.

787 Once the data calibrated, the software attributes if possible each peak to a molecular formula.  
788 The matrix of list of atoms, their isotopes, and number boundaries to be considered for the  
789 final attribution are chosen by the operator; for the present work, given our sample  
790 composition and the mass range investigated we used only the major isotopes ( $^1\text{H}$ ,  $^{12}\text{C}$ ,  $^{14}\text{N}$ ,  
791  $^{16}\text{O}$ ) and arbitrarily limited the number of C atom to be between 1 and 30, the number of H  
792 atoms between 3 and 90, the number of N atoms between 0 and 15, and the number of O  
793 atoms between 0 and 15. Once the constraints given to the software, it computes for each  
794 peak  $m/z$  a list of combinations that span at least  $m/z-1$  to  $m/z+1$  of selected blocks so that  
795 the nitrogen rule is verified and keep attributions. Attribution also takes into account the  
796 charge of the ions and mass of the hydrogen added or loss during the ESI ionization. The  
797 matches within a 5 ppm windows are kept for further investigation. Once the attribution done,  
798 the software checks for the presence of isotopic pattern. For this work we considered every  
799 isotopic peaks expected above a hundredth of the intensity of the base peak and excludes all  
800 possible attribution that do not pass this criterion. The remaining best match (*i.e.* with the  
801 nominal mass the closest of the measured mass) is kept and considered attributed if the error  
802 between nominal and measured mass is under 5 ppm (typical maximal differences in our  
803 measurements were  $\pm 2$  ppm). For each peak whose attribution has been completed, the  
804 software outputs the number of C, H, N and O atoms and the error in ppm between the  
805 nominal mass of the attributed formula and the measured one. If calibration has been  
806 successful, the error in ppm between attribution and nominal masses should be centered

807 around 0 and not depend of the mass of the molecules. The program thus checks for a  
808 tendency in the error, and if a bias is observed, a new calibration-attribution cycle is started.  
809 This step allowed to attribute molecular formulae to compound detected in the mass spectra  
810 up to  $m/z$  400. A molecule was considered to be present in the sample only if it was detected  
811 in all replicates of the experiment. The list of molecules detected in the sample and used to  
812 produce figures presented in this paper includes both the molecules detected in positive and  
813 negative ionization modes.

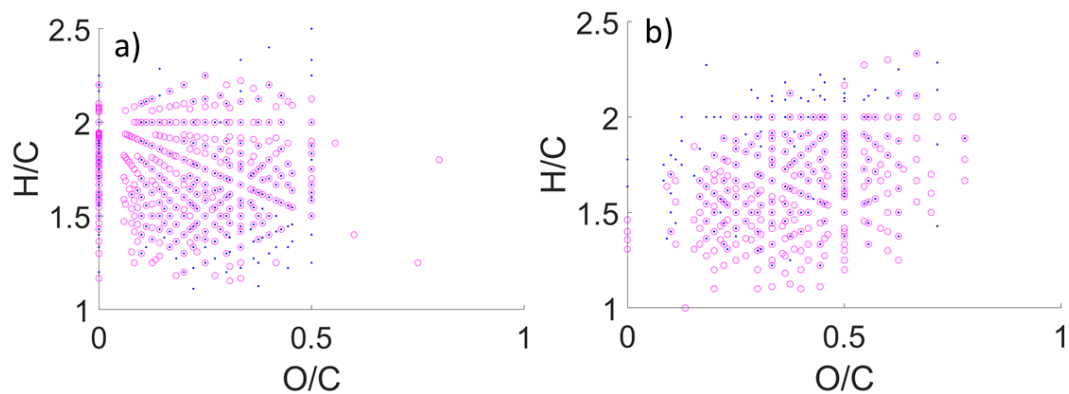
814 *Supplementary Figures:*



815

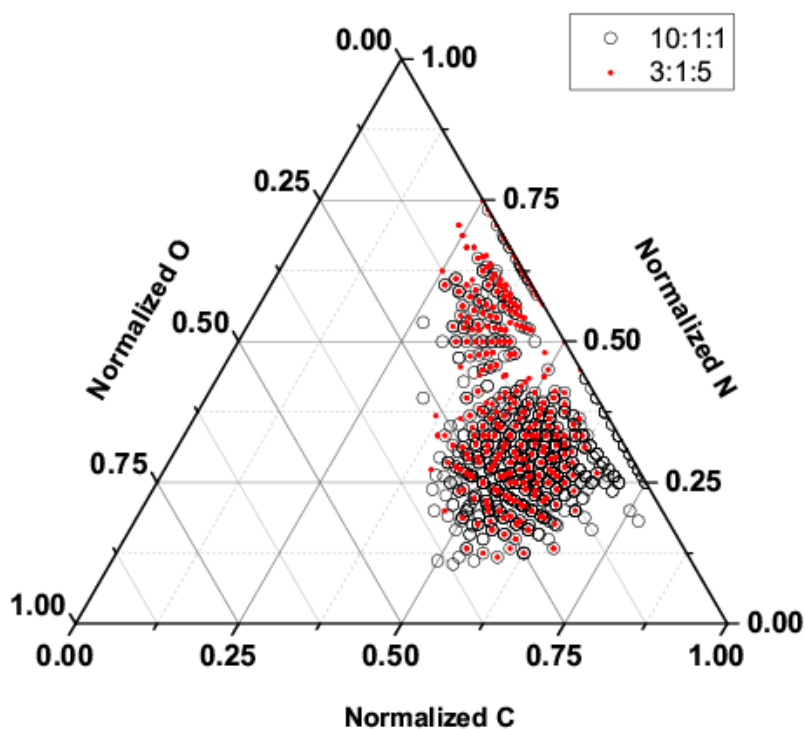
816 **Figure SI 1 : Histogram of Xc for all the molecules detected in the samples.**

817



818

819 **Figure SI 2 :H/C vs O/C van Krevelen plot of the residues formed with 10:1:1 (pink circles) and 3:1:5**  
 820 **(blue dots) H<sub>2</sub>O:CH<sub>3</sub>OH:NH<sub>3</sub> ices for molecules detected in positive (a) and negative (b) ionization**  
 821 **modes.**

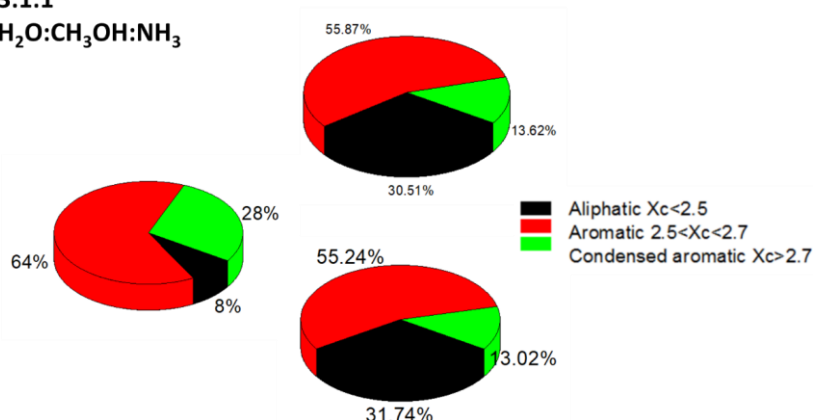


822

823 **Figure SI 3: Ternary plot of the residues formed with 10:1:1 (black circles) and 3:1:5 (red dots)**  
 824 **H<sub>2</sub>O:CH<sub>3</sub>OH:NH<sub>3</sub> ices**

3:1:1

H<sub>2</sub>O:CH<sub>3</sub>OH:NH<sub>3</sub>

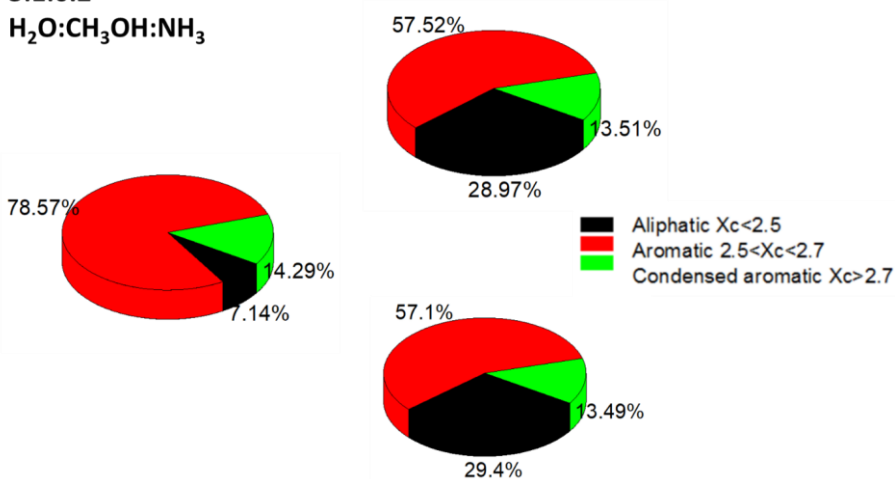


825

826 Figure SI 4 : Repartition of the molecules detected in the 3:1:1 sample depending on their level of  
827 unsaturation based on the evolution of the aromaticity equivalent ( $X_c$ ) for the totality of the  
828 molecules detected in the sample (whole distribution, top chart), the molecules containing C,H,N  
829 and O atoms (CHNO group, bottom chart) and the molecules solely containing C, H and N atoms  
830 (CHN group, left chart). The fraction of molecules classified as aliphatic is shown in black, red  
831 represent the fraction classified as aromatic and green the fraction considered to be condensed  
832 aromatic molecules. The percentage corresponds to the percentage of the molecules classified  
833 according to a given aromaticity relatively to the entire distribution. Given the number of classified  
834 molecules, we can make a conservative estimate of  $\pm 5\%$  as the  $2\sigma$  uncertainties associated with this  
835 classification for the whole distribution.

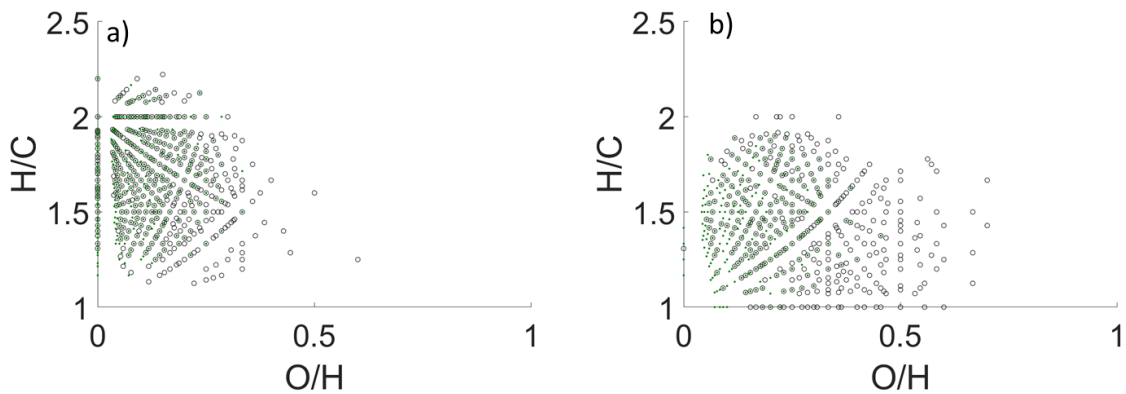
3:1:0.2

H<sub>2</sub>O:CH<sub>3</sub>OH:NH<sub>3</sub>



836

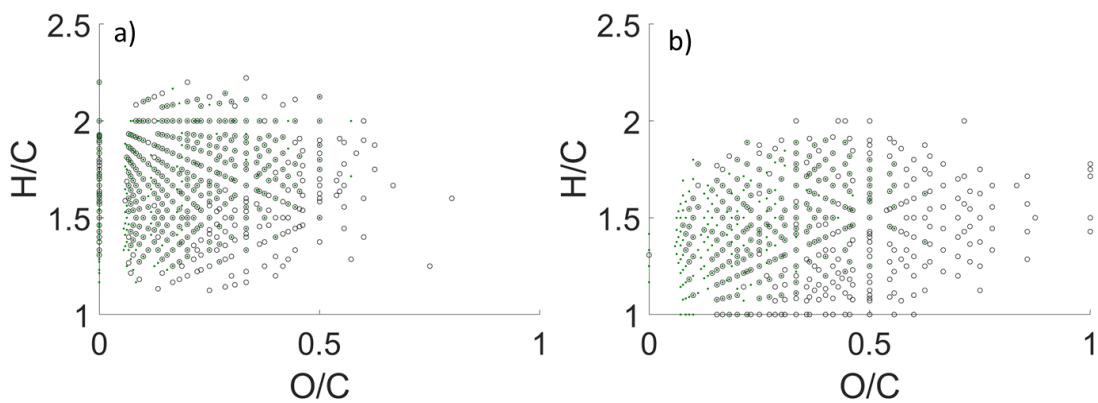
837 Figure SI 5 Repartition of the molecules detected in the 3:1:0.2 sample depending on their level of  
838 unsaturation based on the evolution of the aromaticity equivalent ( $X_c$ ) for the totality of the  
839 molecules detected in the sample (whole distribution, top chart), the molecules containing C,H,N  
840 and O atoms (CHNO group, bottom chart) and the molecules solely containing C, H and N atoms  
841 (CHN group, left chart). The fraction of molecules classified as aliphatic is shown in black, red  
842 represent the fraction classified as aromatic and green the fraction considered to be condensed  
843 aromatic molecules. The percentage correspond to the percentage of the molecules classified  
844 according to a given aromaticity relatively to the entire distribution. Given the number of classified  
845 molecules, we can make a conservative estimate of  $\pm 5\%$  as the  $2\sigma$  uncertainties associated with this  
846 classification for the whole distribution



847

848 **Figure SI 6: O/H vs H/C modified van Krevelen diagram of the molecules detected in the 3:1:1**  
 849 **sample in positive (a) and negative (b) ionization mode before (black circles) and after (green**  
 850 **points) the sample irradiation.**

851



852

853 **Figure SI 7: H/C vs O/C van Krevelen diagram of the molecules detected in the 3:1:1 sample in**  
 854 **positive (a) and negative (b) ionization mode before (black circles) and after (green dots) the**  
 855 **sample irradiation.**

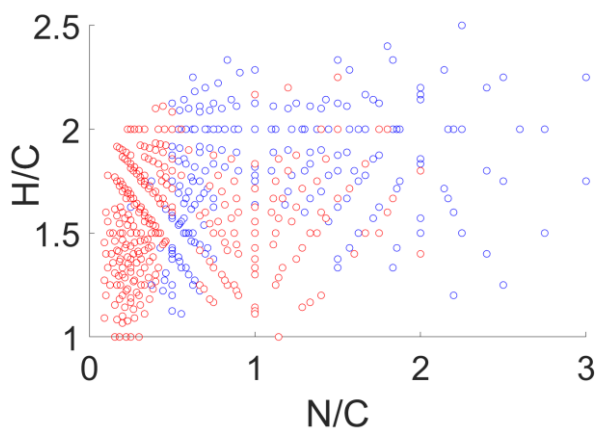


**Figure SI 8 : H/C vs N/C modified van Krevelen diagram of the molecules detected**  
**in the 3:1:5 (blue circles) and 3:1:0.2 (red circles) samples.**